https://doi.org/10.5194/os-2021-121
Preprint. Discussion started: 7 January 2022

Ocean Science
Discussions
Open Access
EGU

Role of wind, mesoscale dynamics and coastal circulation in the interannual variability of South Vietnam Upwelling, South China Sea. Answers from a high resolution ocean model

Thai To Duy [1,2,3], Marine Herrmann[1,2*], Claude Estournel[1], Patrick Marsaleix[1], Thomas Duhaut[1], Long Bui Hong [3], Ngoc Trinh Bich [2]

[1] LEGOS, IRD, UMR5566, IRD/CNES/CNRS/Université de Toulouse, 31400 Toulouse, France

[2] LOTUS Laboratory, University of Science and Technology of Hanoi (USTH), Vietnam Academy of Science and Technology (VAST), 18 Hoang Quoc Viet, Cau Giay, Hanoi, Vietnam

[3] Institute of Oceanography (IO), Vietnam Academy of Science and Technology (VAST), Nha Trang, Vietnam

Correspondence to : Marine Herrmann (marine.herrmann@ird.fr)

https://doi.org/10.5194/os-2021-121
Preprint. Discussion started: 7 January 2022

Ocean Science
Discussions
Open Access
EGU

Short summary

The summer South Vietnam Upwelling develops in the South China Sea, under the influence of monsoon winds. Cold, nutrient-rich waters rise to the surface, where photosynthesis occurs. This biologically active area is essential for the fishing activity. We have developed a very high resolution model to better understand the factors that drive the variability of this upwelling, along the coast and offshore: summer mean to daily chronology of wind, mesoscale ocean dynamics to coastal circulation.

Abstract.

The South Vietnam Upwelling (SVU) develops in the South China Sea off the Vietnamese coast under the influence of southwest monsoon winds. A very high resolution configuration (1 km at the coast) of the SYMPHONIE model was developed over the western coastal region of the South China Sea. A simulation was performed over the period 2009-2018 to study the functioning, variability and influence of oceanic circulation and hydrology in the coastal region, in particular of the SVU. The realism of the simulation in terms of representation of ocean dynamics and water masses, from daily to interannual and coastal to regional scales, is assessed here in detail by comparison with available satellite data and 4 sets of in-situ observations. The interannual variability of the SVU is examined for its 4 main development areas: the southern (SCU) and northern (NCU) coasts, the offshore area (OFU), and the Sunda Shelf area off the Mekong Delta (MKU). For the SCU and OFU, our results confirm the driving role of the summer mean wind and the summer circulation over the offshore area in the interannual variability of the upwelling intensity. They moreover reveal the impact of the spatial and temporal organization of mesoscale ocean structures and high frequency atmospheric forcing. For the NCU, the upwelling interannual variability does not seem to be related to regional scale forcing and dynamics, but is mainly determined by coastal mesoscale structures and circulation : similar summer wind conditions can be associated with very contrasting NCU intensities, and vice versa, depending on the circulation in the NCU area. Finally, our study reveals that upwelling also develops off the Mekong Delta, with an interannual variability mostly determined by the summer wind and the wind-driven circulation over the SVU region.

https://doi.org/10.5194/os-2021-121
Preprint. Discussion started: 7 January 2022


Ocean Science
Discussions
Open Access
EGU

1. Introduction

Ocean circulation in the South China Sea (SCS), one of the largest semi-enclosed seas in the world (Figure 1), is under the influence of several factors of variability at different scales (typhoons, seasonal monsoon, interannual to decadal variability, climate change, Wyrtki 1961, Herrmann et al. 2020, 2021). SCS is moreover impacted by human activities, with highly densely populated coastal areas (CIESIN 2018), which generate problems such as marine pollution (release of industrial, agricultural or domestic contaminants, such as pharmaceuticals, pesticides, heavy metals, plastics …). Reciprocally, coastal societies are highly dependent on marine resources (fisheries and aquaculture, tourism…). SCS also contributes to the functioning and variability of regional climate through air-sea coupling (Xie et al. 2003,2007, Zheng et al. 2016) but also of global climate through its role in the transformation of surface water masses of the global ocean circulation (South China Sea Throughflow, Fang et al. 2009, Qu et al. 2009). It is therefore essential to better understand and model the full range of SCS ocean dynamics at different scales which intervene in the transport and fate of water masses, in the water and energy cycle, in the functioning of planktonic ecosystem (via their impact on the transport and mixing of nutrients and organic matter, Ulses et al. 2016, Herrmann et al. 2017), and in the propagation of contaminants at sea.

The large-scale summer circulation over the SCS is usually characterized by an overall anticyclonic circulation resulting from southwest summer monsoon winds (Wang et al. 2004). It is composed more precisely of a western boundary current and a dipole structure that develops along the Vietnamese coast, with an anticyclonic gyre (AC) in the south and cyclonic gyre (C) in the north. This dipole structure induces northward/southward alongshore coastal currents which are the western components of the AC/C gyres, and a marked eastward offshore jet that develops in the area of convergence of both coastal currents and between both gyres, around ~12°N (Xu et al. 1982, Fang et al. 2002, Xie et al. 2003,2007, Chen and Wang 2014, Li et al. 2014, 2017).

Summer wind forcing and this resulting large-scale circulation induce the South Vietnam Upwelling (SVU), one of the main components of the SCS summer ocean dynamics. The SVU strongly influence halieutic resources through its impact on bio-productivity (Bombar et al. 2010, Loick et al. 2007, Loisel et al. 2017, Lu et al. 2018) and affects regional climate (Xie et al. 2003, Zheng et al. 2016). It is driven at the first order by atmospheric forcing, namely Ekman transport and pumping induced by the southwest monsoon wind (Xie et al. 2003). It is moreover reinforced by the eastward jet that enhances the offshore advection of coastal water (Dippner et al. 2007) and by the combination of wind-induced Ekman pumping and positive surface current vorticity associated with cyclonic eddies in the offshore area (Da et al. 2019, Ngo et al. 2021).

Previous field campaigns (Dippner et al. 2007, Bombar et al. 2010, Loick-Wilde et al. 2017), satellite observations (Xie et al. 2003, Kuo et al. 2004, Ngo and Hsin 2021) and modeling studies (Li et al. 2014, Da et al. 2019), showed that the SVU can strongly vary from one year to another. This interannual variability depends in particular on the intensity of the summer monsoon southwest wind and on ENSO, but also on cross-equatorial winds (Wu et al. 2019) and decadal climate variability (Wang et al. 2020). Two recent studies used long simulations or datasets to establish statistical relationships between the interannual variability of SVU intensity, the atmospheric forcing and the background circulation. Da et al. (2019), using a 1/12° (9 km) 14-years simulation, and Ngo and Hsin (2021), based on ¼° (28 km) datasets of 38-years SST and reanalysis winds and 28-years satellite-altimeter derived sea surface current, showed that the upwelling develops both along and offshore the Vietnamese coast. They quantified the link between the interannual variability of the southern

https://doi.org/10.5194/os-2021-121
Preprint. Discussion started: 7 January 2022

coastal and offshore upwellings and the intensity of the summer ocean circulation (eastward jet, AC/C dipole and associated northward/southward boundary currents) induced by the summer monsoon wind. These studies moreover showed that upwelling sometimes develops along the northern part of the coast from 11°N to 15°N. Da et al. (2019) also revealed and quantified the important contribution of ocean intrinsic variability (OIV) in the SVU interannual variability in the offshore area, mainly related to the role of vorticity associated with mesoscale structures of strongly chaotic nature. Chen et al. (2012) moreover showed that tides and river plumes could be additional mechanisms involved in SVU dynamics.

Most of previous studies were based on numerical or observational datasets associated with several methodological choices and hypothesis : short study periods and limited spatial coverage of in-situ datasets, models resolution not finer than ~10 km, cloud cover and proximity of the coast hindering satellite data quality, gridded current datasets built from along-track sea level satellite data that can not capture small scale and non-geostrophic dynamics, synoptic view based on spatially and seasonally integrated indicators, no or simplified representation of tides and river plumes… This limited their ability to capture or represent the full range of scales involved in the SVU variability, which goes from regional circulation to submesoscale and coastal dynamics and from daily to interannual variability. Further investigations are therefore needed to better understand the role of these processes at different scales and their interactions, in order to improve our knowledge of ocean dynamics and its impacts in the SCS and VNU regions. Numerical modeling is a valuable tool for that.

The objective of the work presented here is therefore both methodological and scientific. With the goal of better modeling and understanding the functioning, variability and influence of ocean dynamics in this area, we developed a very high resolution configuration of a numerical ocean model, able to represent ocean dynamics and water masses at all scales from the Vietnamese coast to the offshore region. This numerical tool is presented in Part 2, and its ability to represent ocean dynamics and water masses is evaluated in Part 3. We then used this tool to examine the variability of the SVU at different scales. Here we first focus on its interannual variability over its 4 main areas of development, examining in particular the role of high frequency and small scale dynamics. This analysis is presented in Part 4. Results are summarized in Part 5.

2. Methodology : numerical tool and observation datasets

2.1. The regional ocean hydrodynamical model SYMPHONIE

The 3-D ocean circulation model SYMPHONIE (Marsaleix et al. 2008, 2019) is based on the Navier-Stokes primitive equations solved on an Arakawa curvilinear C-grid under the hydrostatic and Boussinesq approximations. The model makes use of an energy conserving finite difference method described by Marsaleix et al. (2008), a forward-backward time stepping scheme, a Jacobian pressure gradient scheme (Marsaleix et al. 2009), the equation of state of Jackett et al. (2006), and the K-epsilon turbulence scheme with the implementation described in Michaud et al. (2012) and Costa et al. (2017). Horizontal advection and diffusion of tracers are computed using the QUICKEST scheme (Leonard 1979) and vertical advection using a centered scheme. Horizontal advection and diffusion of momentum are each computed with a fourth order centered biharmonic scheme as in Damien et al. (2017). The biharmonic viscosity of momentum is calculated according to a Smagorinsky-like formulation derived from Griffies and Hallberg (2000). The lateral open boundary

https://doi.org/10.5194/os-2021-121
Preprint. Discussion started: 7 January 2022

conditions, based on radiation conditions combined with nudging conditions, are described in Marsaleix et al. (2006) and Toublanc et al. (2018). The VQS (vanishing quasi-sigma) vertical coordinate described in Estournel et al. (2021) is used to avoid an excess of vertical levels in very shallow areas while maintaining an accurate description of the bathymetry and reducing the truncation errors associated with the sigma coordinate (Siddorn et al. 2013).

The configuration used in this study is based on a standard horizontal polar grid (Estournel et al. 2012) with a resolution decreasing linearly seaward, from 1 km at the Vietnamese coast to 4.5 km offshore (Figure 1), and 50 vertical levels. This configuration zoomed on the Viet Nam coast is hereafter referred to as the VNC configuration. The simulation runs from January 1st, 2009 to December 31st, 2018. The atmospheric forcing is computed from the bulk formulae of Large and Yeager (2004) using the 3-hourly output of the European Center for Medium-Range Weather Forecasts (ECMWF) 1/8° atmospheric analysis, distributed on http://www.ecmwf.int. Initial ocean conditions and lateral ocean boundary conditions are prescribed from the daily outputs of the global ocean 1/12° analysis distributed by the Copernicus Marine and Environment Monitoring Service (CMEMS) on http://marine.copernicus.eu. The implementation of tides follows Pairaud et al. (2008, 2010). It includes tidal amplitude and phase introduced at open lateral boundaries and the astronomical plus loading and self-attraction potentials, and considers the 9 main tidal harmonics, provided by the 2014 release of the FES global tidal model (Lyard et al. 2006). As the absence of tides in the 3D COPERNICUS simulation led to an underestimation of T and S mixing near the bottom, we add to the COPERNICUS fields the effect of the tidal mixing effect, using the parameterization described in Nguyen-Duy et al. (2021). The boundary conditions for rivers are described in Reffray et al. (2004) and Nguyen-Duy et al. (2021). 3 kinds of river runoff data were available over the region : monthly climatology data for 17 rivers, yearly climatology data for 1 river, and daily real-time data for 18 rivers (see Figure 1 for locations of river mouths). The total freshwater discharge of the 36 rivers is equal on average over 2009-2018 to 21.4. 10^3 m^3s^{-1}. To account for the interannual variability of river discharges for climatological data, we applied to those climatological data a yearly multiplying coefficient obtained from daily data time series.

2.2. Observation data

2.2.1. Satellite data

Available satellite observations are used to evaluate the ability of our model to reproduce sea surface characteristics over the study area. For model-data comparisons, model outputs are interpolated on spatial and temporal grids of satellite data:

- OSTIA (Operational Sea Surface Temperature and Sea Ice Analysis) level 4 analysis daily SST produced using an optimal interpolation approach by the Group for High Resolution SST (GHRSST, UK MetOffice, 2005) on a global 0.05° grid over the period 2009-present, available at ftp://data.nodc.noaa.gov/pub/data.nodc/ghrsst/L4/GLOB/UKMO/OSTIA/.

- Boutin et al. (2018) version 3 of 9-day-averaged level 3 SSS produced from SMOS microwave imaging radiometer with aperture synthesis (MIRAS) at a 0.25° resolution over 2010-2017, available at ftp://ext-catds-cecos-locean:catds2010@ftp.ifremer.fr.

- Daily altimetry sea level (SSH) data produced by AVISO (Archiving, Validation and Interpretation of Satellite Oceanographic data) at a 0.25° resolution over the period from 1993 up to now (Ablain et al. 2015, Ray and Zaron 2015), distributed by the CMEMS on http://marine.copernicus.eu. For both simulated and observed time series, the daily

https://doi.org/10.5194/os-2021-121
Preprint. Discussion started: 7 January 2022

altimetry sea level anomaly (SLA) is obtained by removing at each point the SSH temporal average over 2009-2018 : $SLA(x,y,t) = SSH(x,y,t) - \underline{SSH(x,y,t)}$

2.2.2. In-situ data

To evaluate the ability of the model to reproduce hydrological characteristics of water masses, we collected and processed temperature and salinity in-situ data available over the study area (see measurements characteristics in Table 1 and locations in Figure 2). For comparison purposes, modeled outputs are spatially and temporally co-localized with observational data:

- ARGO floats : over the period 2009-2018 more than 3 600 profiles were collected in our study area, available on ftp://ftp.ifremer.fr/ifremer/argo/geo/pacific_ocean/

- Sea-glider Vietnam – US campaign : under the framework of a cooperative international research program, including Vietnamese and U.S. scientific institutions (Rogowski et al. 2019), a glider-based observational program was initiated. Seaglider sg206 was deployed on 22 Jan 2017 and crossed the southward currents near the shelf break approximately 4 times before the steering mechanism malfunctioned on 21 Apr 2017. Ultimately, the mission ended on 16 May 2017 without recovery. The glider collected 552 vertical profiles over the 114 days of deployment (hereafter called GLIDER data).

- ALIS R/V data : the VITEL cruise was organized in May – July 2014 on the French scientific vessel ALIS (P.I S. Ouillon, funding CNES/TOSCA). During the trajectory of the ALIS vessel in the SCS, surface temperature and salinity were measured every 6 seconds, from 10 May 2014 to 28 July 2014 by the automatic thermosalinometer Seabird SBE21 (hereafter called ALIS-TSG data).

- IO-18 data : Meteorological, current, temperature, and salinity parameters were measured in the framework of the Vietnamese State project (code DTDL.CN-28/17, PI. Vo Si Tuan) in September 2018. Measurements were performed by a Sea-Bird 19plus CTD at 19 stations, including 16 instantaneous measurement stations and 3 stations where measurements were collected every 3 hours during 24 hours, producing 43 T,S profiles.

2.3. Definition of upwelling areas and indicators

Figure 2 shows the simulated and observed SST averaged over the period of SVU, June-September (JJAS), over 2009-2018. Low SST (< 29°C) simulated by SYMPHONIE and observed in OSTIA along and off the central Vietnam coast is the signature of the SVU, and reveals the same areas of upwelling as Da et al. (2019) and Ngo and Hsin (2021). The coldest water around 109°E - 11.5°N (<27°C at the coast) corresponds to the coastal center of the upwelling. The coastal area of cold water (~28-29°C) extends south and north of this cold center, from 8.8°N, off the Mekong mouth, and to 15.5°N, along the Vietnamese coast. Cold water is also observed offshore, from 109°E to 114°E and from 10°N to 14°N. We therefore define four areas of upwelling, shown in Figure 2 (see caption for exact coordinates). BoxSC corresponds to the well-known coastal upwelling that develops under the effect of the eastward jet, named SCU hereafter. BoxOF corresponds to the offshore upwelling, OFU. BoxNC shows the northern coastal area between 12°N and 15°N where the

https://doi.org/10.5194/os-2021-121
Preprint. Discussion started: 7 January 2022

upwelling develops less frequently and has been much less studied, named NCU hereafter. A fourth area of minimum SST is also visible both in observed and simulated summer SST off the Mekong Delta, in the wake of Con Dau Island between 8° and 10°N and 106.5°E and 109°E, named BoxMK hereafter. To our knowledge this upwelling, named MKU hereafter, was not studied until now. It was however already visible in AVHRR SST data over 1991-2004 (Da et al. 2019, their Figure 1) and in SODA reanalysis SST over 1987-2008 (Fang et al. 2012, their Figure 5).

To examine the interannual variability of the upwelling over each area, we compute from our simulation a SST-based upwelling index for each box, following the methodology detailed in Da et al. (2019). First, for each upwelling area we define the reference temperature T_{RefN} as the 2009-2018 average of SST over the reference box *refN* and over June to September (JJAS). The reference box is taken as the area next to the upwelling box not impacted by surface cooling. Reference boxes are shown in Figure 2. The threshold temperature below which upwelling happens, *To* = 27.6°C, is defined from the frequency of occurrence of cold surface water as the temperature allowing to cover the largest number of upwelling occurrences but avoiding to consider cold water advected between areas. To estimate the strength of the upwelling over the area *boxN*, we define the daily index of upwelling :

$$UI_{d,boxN}(t) = \frac{\iint_{(x,y)in\ boxN\ so\ that\ SST(x,y,t)<To}(T_{refN}-SST(x,y,t)).dx.dy}{A_{boxN}} \quad (1)$$

where A_{boxN} is the size of *boxN*. We also define the yearly index :

$$UI_{y,boxN} = \frac{\int_{JJAS} UI_{d,boxN}(t)dt}{ND_{JJAS}} \quad (2)$$

where ND_{JJAS} is the duration of the JJAS period. To examine the spatial distribution of the upwelling, we also introduce a spatially dependent index of upwelling :

$$UI_{S,boxN}(x,y) = \frac{\int_{t\ in\ JJAS\ so\ that\ SST(x,y,t)<To}\left(T_{refN}-SST(x,y,t)\right)dt}{ND_{JJAS}} \quad (3)$$

3. Model evaluation

3.1. Representation of surface circulation and hydrological characteristics

Figure 3 shows the time series of climatological monthly and interannual yearly averages of simulated and observed SST, SSS and SLA averaged over the VNC domain. The normalized root-mean square error of a simulated time series compared to an observed time series is computed as $NRMSE = \frac{\sqrt{\frac{1}{N}(\sum_{i=1}^{n}(S_i-O_i)2}}{O_{max}-O_{min}}$ where S_i and O_i are respectively the simulated and observed values, and O_{max} and O_{min} the maximum and minimum observed values. Figure 4 shows the maps of winter and summer climatological average over 2009-2018 of observed and simulated SST, SSS and SLA.

https://doi.org/10.5194/os-2021-121
Preprint. Discussion started: 7 January 2022

3.1.1. Annual Cycle and seasonal variability

The simulated seasonal cycle of SLA is in very good agreement with AVISO observations (Figure 3e), with a 1.0 correlation coefficient ($p < 0.01$) and a 6% NRMSE. It is maximum in November-January and minimum in June-July, in agreement with studies made from TOPEX/Poseidon altimeter data on the seasonal variability of SLA over the SCS between 1992 and 1997 by Shaw et al. (1999) and Ho et al. (2000). Winter and summer SLA spatial patterns are realistically reproduced (Figure 4,i,j,k,l), with highly significant spatial correlations between simulated and observed fields ($R>0.98$). As explained in the Introduction, northeast monsoon winds induce a basin-wide cyclonic geostrophic circulation in winter. In summer, southwest monsoon winds induce a globally anticyclonic geostrophic circulation with a northward alongshore current. At a finer spatial scale, this current is composed of several gyres, in particular two anticyclonic (AC) gyres centered at ~11°N and ~16°N and a cyclonic (C) gyre centered at ~13°N. The 11°N AC and 13°N C gyres form the well-known dipole and associated eastward jet (Wyrtky 1961, Xu et al. 1982, Fang et al. 2002, Xie et al. 2003,2007, Chen and Wang 2014, Li et al. 2014, 2017).

The seasonal cycle of SST over the region is very well reproduced by the simulation (Figure 3a). The bias compared to OSTIA data is equal to 0.08°C on average, and varies between 0.02°C in winter and 0.09°C in summer, with a 2% NRMSE and a highly statistically significant correlation (1.0, $p<0.01$). Under the influence of Southeast Asia Monsoon, SST is maximum in May-June and minimum in January-February. This is consistent with Siew et al. (2013), who characterized the monthly climatological SST in the area from HadISST observations and 10 coupled model runs over the period 1961-2000. SST spatial patterns are also realistically simulated, with highly significant spatial correlations between simulated and observed fields (Figure 4a,b,c,d, $R=0.99$ in winter and 0.85 in summer). In winter, the cold atmospheric fluxes and basin wide cyclonic circulation result in a strong meridional SST gradient, with coldest waters in the north and a cold tongue (SST< 26 °C) extending southward along the Vietnamese coast. In summer, the upwelling developing along the Vietnamese coast and extending offshore is clearly visible from the SST minimum (<28°C) on observed and simulated datasets. Though SYMPHONIE is overall in very good agreement with OSTIA in terms of spatial variability and temperature range, it however slightly overestimates the observed surface cooling in very coastal areas near Hainan and southern Vietnam coasts. Piton et al. (2021) suggested that this surface cooling could be induced by tides. This difference could also be partly explained by the SST smoothing in OSTIA, as shown by Woo et al. (2020).

The simulated SSS over the VNC domain follows well the observed SMOS SSS (Figure 3b), with a highly statistically significant correlation (0.89, $p<0.01$). Our simulation shows a fresh bias (-0.30 on average, from -0.22 in winter to -0.36 in summer), and an associated NRMSE of 0.76. This salinity difference could be due to the coarse resolution of SMOS (28 km), but also to an overestimation of atmospheric freshwater flux in the atmospheric forcing. Spatial patterns are well reproduced, with highly significant spatial correlations between observed and simulated SSS fields (0.84 in winter and 0.88 in summer, $p<0.01$, Figure 4e,f,g,h). Both simulation and data show low SSS over the Gulf of Thailand and the northwestern Gulf of Tonkin, associated with the strong river and atmospheric freshwater fluxes. In the northeastern SCS, they show high SSS round the year, due to the influence of water entering through the Luzon Strait from the Western Pacific Ocean (Qu et al. 2000; Zeng et al. 2016).

https://doi.org/10.5194/os-2021-121
Preprint. Discussion started: 7 January 2022

3.1.2. Interannual variability

The interannual variability of SLA is very well simulated, with a 0.94 ($p<0.01$) correlation coefficient and a 0.13 NRMSE compared to AVISO dataset (Figure 3f). Both observed and simulated datasets show minimum values in 2009, 2011 and 2015, and maximum in 2010, 2012 and 2013, with an amplitude of ~3-4 cm.

The interannual variability of SST is also very well simulated, with a 0.95 ($p<0.01$) correlation coefficient and a 0.13 NRMSE compared to OSTIA dataset (Figure 3b). SST shows strong variations over the period, with a 1°C difference between the coldest (2011, 27.5°C) and warmest (2010, 28.5°C) years. As shown by Yu et al. (2019) over the period 2003-2017, those interannual variations are strongly related to ENSO : the 2010 and 2015-2016 El Niño events induce SST maxima, while the 2011 La Niña event induces a SST minimum.

Simulated interannual SSS time series shows a statistically significant correlation (0.80, $p<0.01$) and a 0.48 NRSME compared to SMOS observations (Figure 3d). Both model and data show an increase between 2012 and 2016, also observed by Zeng et al. (2014, 2018). Through a budget analysis based on a SCS 4 km SYMPHONIE configuration over the SCS, Trinh (2020) attributed this salinification to the rainfall deficit during this period.

3.2. Representation of hydrological characteristics and vertical distribution of water masses, at the daily to interannual scales

We use ARGO, GLIDER, IO-18 and ALIS-TSG datasets to evaluate the ability of the model to reproduce water masses over the VNC domain, from the regional open-sea scale to the coastal scale. For that, we examine T-S diagrams built from ARGO (Figure 5a), GLIDER (Figure 5b) and IO-18 (Figure 5c) observations and colocalized SYMPHONIE outputs.

At the regional scale, ARGO data cover the whole open-sea region over 2009-2018. The hydrological characteristics and vertical distribution of water masses defined by Uu and Brankard (1997) and Dippner et al. (2011) (see Figure 5a) are overall very well simulated, with very similar contours of simulated and observed scatterplots. First, it reproduces the whole range of surface water masses, with salinity varying between 32 and 34 and temperature between 20°C and 30°C : the fresh MKGTW (Mekong and Gulf of Thailand Water), the more saline OWW (Offshore Warm Water) and OSW (Offshore Salty Water) and the colder ECSW (East China Sea Water). Second, it reproduces realistically the observed salinity maximum (reaching ~34.8) that corresponds to the Maximum Salinity Water (MSW, between 100 and 200m depth) and the salinity minimum (reaching ~34.4) that corresponds to the Permanent Thermocline Water (PTW, at ~400 m depth). Last, it reproduces correctly the Deep Water (DW) mass, with a cold average bias (0.1°C) and a negligible salinity bias (<0.01).

GLIDER data were collected between January and May 2017, i.e. during the period of northeast monsoon and the transition period to the southwest monsoon. They cover the regional to coastal scales (Figure 1b). During this 9th year of the simulation, the model is able to reproduce in detail the observed temperature and salinity profiles (Figure 5b), though with slightly higher biases of salinity (up to 0.15) and temperature (up to 0.4°C) than for ARGO dataset. In particular it reproduces realistically not only the deep water masses down to 1000 m depth, but also the 2 branches of surface water masses that were sampled by the glider : the fresher branch (SSS<34.5) observed at the beginning of the glider cruise south of 16°N, and the warmer branch (reaching 20°C) observed at the end of the cruise north of 17°N (see Figure SM1 that shows the observed and simulated SSS and SST along the trajectory). SYMPHONIE is therefore able to capture the

https://doi.org/10.5194/os-2021-121
Preprint. Discussion started: 7 January 2022

variability of water masses over the winter to summer transition period, from the coastal to more open-sea area, without producing a significant drift after more than 8 years of simulation.

IO-18 and ALIS data were collected during the period and over the region of upwelling, respectively in 2014 and 2018. Figure 6 shows the values of observed and colocalized simulated sea surface temperature and salinity along the ALIS-TSG trajectory, and their bias. The high frequency variability of SST and SSS recorded by the TSG along the ALIS trajectory during summer 2014 is very well simulated, with a 0.89, resp. 0.93, correlation between observed and simulated time series. In particular both observed and simulated outputs clearly reveal the surface cooling (by more than 1 °C, with water colder than 28°C) and saltening (sith salinity reaching 34) observed at the end of June - beginning of July 2014 in the SVU area. IO-18 cruises covered both the shallow shelf area (8 stations, Figure 1) and the coastal to offshore upwelling area (10 stations) during summer 2018. The coastal shallow region, submitted to the influence of the Mekong freshwater, shows warm (> 27°C) and fresh (<34) water, corresponding to the nearly horizontal branch of the T-S diagram (Figure 5c). In the deeper offshore region the water is much colder and saltier (<20°C and > 34.5, the nearly vertical branch). Again, the model reproduces well the temperature and salinity characteristics of both types of water masses and areas. It is therefore able to reproduce the diversity of profiles in the coastal and offshore upwelling region without any significant bias, even after 9 years of simulation.

4. Interannual variability of the South Vietnam Upwelling

Our high-resolution simulation reproduces realistically the surface circulation and the hydrological characteristics of water masses at the surface and over the water column, and their spatial (from shelf to open sea) and temporal (seasonal to interannual) variability. Based on this 10-years simulation, we examine in detail the functioning and interannual variability of SVU over the 4 regions of interest : southern (BoxSC) and northern (BoxNC) coasts, offshore region (BoxOF) and Sunda shelf (BoxMK). Figure 7 shows the time series of yearly upwelling index over the period 2009-2018 for the 4 boxes. Table 2 shows the mean and standard deviation of those time series, the coefficient of variation CV defined as the ratio between the standard deviation and mean, and correlations between time series of significant factors, in particular upwelling yearly indexes and summer wind. Figure 8 shows for each year of the simulation the maps of spatial upwelling index $UI_{S,boxN}$ and of JJAS averaged surface current and of its vorticity.

4.1. BoxSC

As already shown in previous studies cited above, the SCU develops along the Vietnamese coast between 10.5°N and 12°N in the area of convergence between the northern southward and southern northward boundary currents (Figure 8). These currents are associated with respectively the northern cyclonic and southern anticyclonic gyres, and their convergence results in the eastward jet.

SCU shows a significant interannual variability, though the lowest of the 4 boxes (CV = 53%, Table 2). Previous studies suggested that the interannual variability of upwelling in the coastal area of Vietnam is mainly triggered by the interannual variability of the summer averaged wind stress that induces Ekman transport (Chao et al. 1996, Dippner et al. 2007, Da et al. 2019, Ngo and Hsin 2021). Figure 7 shows the yearly time series of the average over each box and over JJAS of wind stress, $WS_{JJAS,boxN}$. First, time series of the summer wind over BoxSC and over BoxOF are almost equal (Figure 7) and completely correlated (0.99, $p<0.01$, Table 2). The intensity and interannual variability of summer wind over boxSC is thus completely driven by the large-scale wind. Second, in 2010, $WS_{JJAS,SC}$ is minimum and significantly weaker than

https://doi.org/10.5194/os-2021-121
Preprint. Discussion started: 7 January 2022

for the other years and almost no upwelling develops over BoxSC ($UI_{y,SC}$ ≃0.05 °C, one order of magnitude smaller than the average). Conversely, when wind stress peaks in 2018 (WS_{JJAS} ≃0.11 $N.m^{-2}$) SCU also reaches its maximum intensity ($UI_{y,SC}$ ≃1.49 °C, about twice stronger than the average). We moreover obtain a highly significant correlation between $UI_{y,SC}$ and $WS_{JJAS,SC}$ (R=0.85, p<0.01, Table 2). This confirms that the interannual variability of SCU is driven at the first order by the intensity of the summer averaged monsoon wind.

Other factors however modulate the summer wind-induced interannual variability of SCU.

The first factor is the daily to intraseasonal variability of wind forcing. For example, even though 2009 and 2012 show the same average summer wind over BoxSC ($WS_{JJAS,SC}$ ≃0.09 $N.m^{-2}$, Figure 7), SCU is 23% weaker in 2009 ($UI_{y,SC}$ ≃0.73 °C, Figure 7) than in 2012 ($UI_{y,SC}$ ≃0.95 °C). Figure 9 shows the time series of daily upwelling index $UI_{d,SC}$ and of daily average wind stress over boxSC for 2009 and 2012 (and 2011). For all the years, the development of upwelling over BoxSC is related to the daily chronology of wind, with upwelling peaks occurring during wind peaks. The wind over BoxSC is stronger in July and September for 2009, vs. June and August for 2012. In 2012, the SCU consequently develops strongly in June, and persists throughout the summer, especially in August. Conversely in 2009 it mainly develops in July, and does not persist in August due to the weaker wind during this month. The daily to intraseasonal variability of wind forcing during the summer therefore modulates the SCU interannual variability.

High frequency wind forcing however does not explain all the differences. The coastal circulation and mesoscale dynamics also contribute to the modulation of the SCU intensity. For example, 2011 shows the second strongest SCU ($UI_{y,SC}$ ≃1.35 °C, Figure 7), ~90% stronger than for 2009 and ~40% than for 2012. However, $WS_{JJAS,SC}$ in 2011 (≃0.09 $N.m^{-2}$, Figure 7) is ~10% lower than in 2009 and 2012. Moreover, wind stress in June 2011 is not stronger than in June 2009 and 2012, neither in average nor in terms of high frequency peaks (Figure 9). However, SCU develops strongly in June 2011 and persists throughout the summer, reaching much higher values than in 2009 and 2012. This suggests that the higher upwelling intensity in 2011 is not related to a difference in summer wind, neither in average nor at the daily to intraseasonal scales. Instead, it is related to the background circulation (Figure 8). 2009 and 2012 show the double AC/C dipole and associated eastward jet at ~12°N classically described in the literature. Instead, 2 AC/C dipoles develop during summer 2011 along the Vietnamese coast, one southern than for the other years, and one northern. They result in 2 eastward jets departing respectively from ~11°N and 14°N. This results in an overall offward current along the coast, hence in a wider coastal upwelling. The background coastal circulation and mesoscale structures are therefore a second factor that modulates the SCU interannual variability.

4.2. BoxOF

The interannual chronology of wind stress and summer upwelling over BoxOF is very similar to that of BoxSC (Figure 7), with a minimum in 2010 and a maximum in 2018. $UI_{y,SC}$ and $UI_{y,OF}$ are highly significantly correlated (0.73, p=0.02, Table 2). This suggests that the interannual variability of OFU and of SCU are driven by the same factors. The summer wind strength indeed is a key factor involved in OFU interannual variability : $UI_{y,OF}$ and $WS_{JJAS,OF}$ are highly statistically significantly correlated (R = 0.77, p=0.01, Table 2) though slightly less than for SCU (0.85). OFU shows the strongest interannual variability (CV≃126%, Table 1), explained partly by the very strong OFU in 2018 compared to other years, related to the strong wind in summer 2018 (Figure 7).

https://doi.org/10.5194/os-2021-121
Preprint. Discussion started: 7 January 2022

Da et al. (2019) simulated an Ekman pumping-related OFU that develops under the influence of strong positive wind curl, that can be enhanced (weakened) if cyclonic (anticyclonic) mesoscale structures associated with positive (negative) surface current vorticity are present in the area of positive wind curl. The influence of those chaotic mesoscale structures explained the significant impact of OIV in OFU variability. Ngo and Hsin (2021) showed that OFU is stronger (weaker) for years of stronger (weaker) wind stress curl and large scale circulation (eastward jet and dipole). Figure 7 shows the time series of $\zeta_{+,OF}$, the spatial integral over BoxOF of the positive part of summer averaged relative vorticity. It integrates both the cyclonic activity north of the jet and the positive vorticity on the northern flank of the eastward jet (a more intense and narrow eastward current being characterized by a higher vorticity). $\zeta_{+,OF}$ is thus an indicator of the intensity of the summer circulation (dipole+eastward jet) in the offshore region. The interannual variability of this intensity is actually strongly induced by the variability of wind forcing : there is a highly significant correlation between time series of $\zeta_{+,OF}$ and $WS_{JJAS,OF}$ (0.89, $p<0.01$, Table 2).

Our high-resolution simulation confirms the link between the intensity of OFU and of summer offshore circulation and related vorticity. OFU indeed occurs mainly in areas of positive surface current vorticity : along the northern flank of the eastward jet and north of the jet as the result of mesoscale cyclonic structures (Figure 8). For example, wind is similar for 2014 and 2016 ($WS_{JJAS,OF} \simeq 0.08$ N.m^{-2}, Figure 7), however OFU is about twice stronger in 2014 (0.06°C) than in 2016 (0.03°C). The difference can be explained by the mesoscale activity and eastward jet in the offshore area. In 2014, an intense cyclonic eddy forms north of the intense and marked eastward jet (Figure 8), and $\zeta_{+,OF}$ is twice larger (~2.6×10^{-6} s^{-1}, Figure 7) than in 2016 (~1.5×10^{-6} s^{-1}). In 2016 the jet is indeed wide and less intense and no cyclonic eddy develops. The significant correlation between time series of $UI_{y,OF}$ and $\zeta_{+,OF}$ (0.69, $p=0.03$, Table 2) quantifies this link between OFU intensity and the intensity of summer offshore circulation. $UI_{y,SC}$ is also significantly correlated with $\zeta_{+,OF}$ (0.60, $p=0.07$, Table 2), which confirms that SCU is stronger/weaker for years of intense/weak summer circulation off Vietnam coast.

For some cases, as suggested by Ngo and Hsin (2021), OFU can even be inhibited. In 2010 upwelling does practically not develop over BoxOF and BoxSC (Figure 7). The eastward offshore jet and dipole structure that are usually observed in summer do not exist during summer 2010 ($\zeta_{+,OF}$ ~0.5×10^{-6} s^{-1}, much smaller than for the other 9 years and four times smaller than the mean, Figure 7 and Table 1), and the alongshore current flows northward between 9°N and 16°N (Figure 8). Those circulation conditions prevent the formation of an offshore current and of the associated upwelling. For this year, extreme weak wind conditions as well as circulation background thus both prevent the development of upwelling.
Factors other than summer wind intensity and summer circulation over the offshore area modulate the variability of OFU. For example, in 2018 both $WS_{JJAS,OF}$ (0.11 N.m^{-2}, Figure 7) and $\zeta_{+,OF}$ (3.4×10^{-6} s^{-1}) are only ~10% higher than in 2009 and 2012 (respectively 0.10 N.m^{-2} and 3.1×10^{-6} s^{-1}). However, $UI_{y,OF}$ in 2018 (0.32°C) is respectively 2.6 and 4.6 times larger than in 2009 (0.12°C) and 2012 (0.07°C), and 4 times higher than the average (0.09°C, Table 2). Comparatively, for BoxSC, $UI_{y,SC}$ in 2018 it is only ~2 times larger than the average value. Last, the correlation between $UI_{y,box}$ and $WS_{JJAS,box}$ is lower for BoxOF (0.77) than for BoxSC (0.85). This shows that other factors modulate the interannual variability of OFU, even more than for SCU.

The intraseasonal variability of wind is one of those factors. Figure 10 shows the time series of daily upwelling index $UI_{d,OF}$ and daily average wind stress over boxOF for 2009, 2012 and 2018. Wind stress peaks mostly occur in July and September in 2009, and in June and September in 2012. In contrast, in 2018, wind stress peaks occur in July and August, inducing a very strong upwelling during those months. The monthly averaged wind is consequently significantly stronger

https://doi.org/10.5194/os-2021-121
Preprint. Discussion started: 7 January 2022

in July and August 2018 than in July and August of the other years, and than in June and September 2018 (Figure 10). This suggests that OFU is stronger when wind peaks occur during the core of the summer season (July-August) than at the beginning (June) or end (September). The correlation of time series of $UI_{y,OF}$ with time series of July-August averaged wind stress over BoxOF is indeed higher (0.84, $p<0.01$, Table 2) than the correlation with JJAS wind stress (0.77, $p<0.01$), confirming this hypothesis. Conversely, for BoxSC, this correlation is weaker (0.70, $p=0.03$ for July-August vs. 0.85, $p<0.01$, for JJAS, Table 2). The development of SCU occurs during the whole JJAS period as soon as the wind conditions are favorable, and is thus mainly induced by wind forcing which prevails on and drives circulation patterns. Summer wind forcing also appears to be one of the major factors inducing OFU. However, other factors, presumably related to a favorable combination of wind forcing and background circulation, favor its development during July-August more than June and September.

4.3. BoxNC

Upwelling also develops, though to a weaker extent, along the northern part of the central Vietnam coast (BoxNC). $UI_{y,NC}$ shows a relatively strong interannual variability (71%, Table 2). We obtain no statistically significant correlation between $UI_{y,NC}$ time series and time series of the average wind stress, whatever the period and area of averaging (Table 2). Moreover we obtain no statistically significant correlation between $UI_{y,NC}$ time series on one hand and $UI_{y,SC}$ or $UI_{y,OF}$ time series on the other side (Table 2). This suggests that contrary to SCU and OFU, the interannual variability of NCU is not driven by the summer wind or the summer offshore circulation.

Examining into details the 10 summers of the simulation in Figure 8, we identify 4 main situations that prevent or favor the development of NCU. First, the inhibition of NCU can result from two opposite situations in terms of wind, offshore circulation and upwelling intensity over the other boxes :

- Influence of a marked southward alongshore current : summers 2009, 2012, 2018. Those years show maxima of summer wind over the region (see $WS_{JJAS,OF}$, Figure 7) and of SCU and OFU intensity, but minima of NCU intensity (Figure 7). They are associated with a highly marked dipole and associated eastward jet, with a strong positive vorticity over the offshore area (Figures 7,8). As explained above, those atmospheric and circulation patterns explain the strong SCU and OFU. Moreover, the strong northern cyclonic gyre induces a marked southward alongshore current over BoxNC, with a very weak offshore component. The southward alongshore current is indeed associated with a cyclonic hence divergent circulation, hence with a coastward component and a coastal downwelling. This circulation opposes the wind-induced circulation and inhibits the NCU.

- Influence of a marked northward alongshore current: summers 2010, 2013, 2017. NCU is weaker than average, and SCU and OFU are weaker than average (2010 and 2017) or close to average (2013) (Figure 7). For those 3 cases, summer wind over the region is weaker than the average or average (see $WS_{JJAS,OF}$, Figure 7). This results in weaker than average Ekman transport over the coast and pumping in the offshore region, and much weaker than the average (or even absent in 2010) dipole and eastward jet (see $\boldsymbol{\zeta}_{+,OF}$, Figure 7). Instead, an alongshore northward current with a very weak offshore component develops all along the Vietnamese coast (Figure 8). Those atmospheric and circulation patterns explain the weak OFU, SCU and NCU.

Second, the development of NCU can also result from two different situations:

https://doi.org/10.5194/os-2021-121
Preprint. Discussion started: 7 January 2022

- For some summers (2011, 2014, 2015), a secondary dipole develops north of the usual dipole structure (see the alternation of negative and positive vorticity between 12°N and 16°N, Figure 8). This results in the development of a second coastal area of convergence of northward and southward currents over BoxNC. In addition to the usual eastward jet, a secondary jet thus originates from the northern part of the coast, inducing a strong upwelling over BoxNC. This situation does not seem to be related to the wind intensity : it occurs in case of strong wind and upwelling over BoxOF and BoxSC (2011 and 2014, Figure 7) as in the opposite case (2015). It is also not related to the intensity of summer offshore circulation, which is strong in 2014 (Figure 8) but weak in 2011 and 2015.
- 2016 is the last case : wind over the region, the dipole structure and eastward jet, and, consequently, SCU and OFU, are weaker than average (Figure 7). The eastward current is weaker but also wider than average, and an overall offshore circulation is simulated over a large part of the area (Figure 8). This enhances the offshore advection of cold water from the coast and the development of a stronger than average NCU.

4.4. BoxMK

The interannual chronology of wind stress over BoxMK is very similar to that of BoxOF and BoxSC (Figure 7) and $WS_{JJAS,MK}$ is highly significantly correlated with $WS_{JJAS,SC}$ (0.97, $p<0.01$, Table 2) and $WS_{JJAS,OF}$ (0.96, $p<0.01$). The interannual variability of wind over BoxMK is therefore related to the intensity of the summer monsoon wind over the SVU region.

MKU shows the weakest mean value of the 4 boxes (0.07°C, Table 2), and a relatively strong interannual variability (CV=85%). The interannual chronology of MKU is very similar to that of OFU and SCU, with a minimum in 2010 and a maximum in 2018 (Figure 7). $UI_{y,MK}$ is highly significantly correlated with $UI_{y,SC}$ (0.83, $p<0.01$, Table 2) and $UI_{y,OF}$ (0.92, $p<0.01$). MKU interannual variability is therefore likely driven by the same factors as OFU and, to a slightly lesser extent, SCU.

The summer wind strength and summer offshore circulation are indeed key factors involved in MKU interannual variability. $UI_{y,MK}$ shows a highly statistically significant correlation with July-August wind over the region ($WS_{JA,OF}$: 0.82, $p<0.01$, Table 2). MKU intensity moreover shows highly statistically significant correlation with $\boldsymbol{\zeta}_{+,OF}$ (0.74, $p<0.01$). This correlation is even higher than for SCU and OFU, suggesting an even stronger influence of summer offshore circulation (eastward jet and dipole) in MKU interannual variability.

In contrast with upwelling that develops over the 3 other areas, the position of MKU is very stable from one year to another (Figure 8). It develops in the area of positive vorticity along the western flank of the northeastward current that flows off the Mekong delta, and is stronger when this current is stronger. This current constitutes the western part of the southern anticyclonic gyre of the dipole and forms the eastward jet when it encounters the northern cyclonic gyre. Its intensity therefore varies interannually following the intensity of the summer offshore circulation, explaining the link between MKU and the offshore circulation. However the spatial structure of currents in the MKU region is very stable from one year to another, contrary to what is obtained for the 3 other areas (Figure 8). This suggests that this spatial structure is strongly constrained by non-interannually-varying factors, including topography, and explains the stable position of MKU. BoxMK is indeed located on the shallow continental shelf, with depths varying from ~15 m at the coast to more ~ 200 m over the continental slope (Figure 2).

https://doi.org/10.5194/os-2021-121
Preprint. Discussion started: 7 January 2022

Those results show that MKU interannual variability is presumably driven by the summer monsoon wind and by the northeastward current, which is completely related to the intensity of the wind-induced summer offshore circulation. Moreover, bathymetry related mechanisms in BoxMK constrain the spatial structure of the currents and of MKU, which do not change interannually. For the 3 other boxes, the organization of mesoscale structures and associated vorticity and of coastal circulation modulate the interannual variability of upwelling intensity induced by summer wind. This is not the case for BoxMK.

4.5. Comparison of simulated and observed interannual variability

Ngo and Hsin (2021) produced the most recent and longest time series of observed intensity of upwelling over 3 of the areas studied here (SCU, NCU and OFU), using a SST-based upwelling index applied on a 0.25° dataset of satellite observed SST over the period 1982-2019 (their Figure 4).

For SCU and OFU, the interannual variability of upwelling intensity over the period 2009-2018 is similar at the first order in the time series simulated by our model and observed by Ngo and Hsin (2021) (Figure 7). In particular their intensity is highest in 2018 and lowest in 2010. For SCU, 2011, 2012 and 2014 are more intense than the average in both simulated and observed time series, and 2017 is much less intense than the average. For OFU, 2011 and 2012 are more intense than the average and 2013, 2015, 2016 and 2017 are less intense. However some years are significantly different in simulated and observed time series. 2015 SCU is stronger than average in observations vs. smaller in our simulation. 2009 OFU is lower than average in observations, vs. the 2nd highest in our simulation. Differences are stronger for NCU, with only 4 years in agreement. 2009 and 2012 show particularly weak (or non-existent) NCU, 2015 shows a strong NCU and 2011 an average NCU in both observed and simulated time series.

The low resolution of satellite observations, which are moreover hindered by the strong cloud cover over the region in summer (Gentemann et al. 2004) partly explains those differences, especially in the small coastal boxes BoxNC and BoxSC. They could also be due to the chaotic part of ocean dynamics, which were shown to modulate the wind-induced variability of upwelling over BoxSC, BoxOF and BoxNC. Our results above suggest that this OIV could be stronger for BoxNC, whose interannual variability is more influenced by ocean dynamics than by wind, explaining the larger differences between simulated and observed NCU time series.

5. Conclusion

A configuration of the 3D ocean model SYMPHONIE based on the use of a polar grid (with a high-resolution going from ~1km along the coast to ~4 km in the open sea) and of VQS vertical coordinate was implemented over the Vietnamese coast and offshore SCS to study specific questions over the region (ocean dynamics, impact on ecosystems, propagation of pollutions), taking into account the large range of scales of dynamical processes involved.

We first performed a 10-year simulation over the recent period 2009-2018. Simulated sea surface temperature, salinity and height and vertical salinity and temperature profiles were compared with available satellite data and 4 sets of in-situ observations (ARGO floats (2009-2018), a glider campaign (2017) and 2 R/V campaigns (summers 2014 and 2018)). Those comparisons quantitatively showed the ability of the model to reproduce the ocean circulation and water masses over the region at different scales : from the daily to interannual and climatological scales and from the coastal to regional scales.

https://doi.org/10.5194/os-2021-121
Preprint. Discussion started: 7 January 2022

This simulation was then used to investigate the interannual variability of summer upwelling that develops along the Vietnamese coast. 4 regions of upwelling development were identified : the coastal upwelling, that develops along the southern (SCU) and northern (NCU) parts of the Vietnamese coast, the offshore upwelling (OFU), and an upwelling that develop on the Sunda shelf off the Mekong delta (MKU).

Our results confirmed at the first order the conclusions of Da et al. (2019) and Ngo and Hsin (2021) about the interannual variability of SCU and OFU intensity. This variability is primarily driven by the same processes. The intensity of summer wind stress and curl, which induces Ekman transport and Ekman pumping, is the driving factor at the first order. Moreover, the intensity of summer circulation in the offshore area, i.e. the dipole and associated eastward jet, which is actually also induced by the summer wind forcing, reinforces this wind-induced interannual variability.

The high resolution of the simulation analysed here moreover allowed to reveal and examine the role of other factors, in particular smaller spatial and temporal scales of atmospheric forcing and ocean circulation. First, our results show that the intensity of SCU and OFU is not only driven by the average summer wind, but also by its variability at higher frequency, daily to intraseasonal. For a given summer average wind intensity, SCU is stronger when wind peaks occur regularly throughout the 4 months of the whole JJAS period, compared to situations where peaks occur only during some of the 4 months. Moreover, wind peaks of same intensity induce upwelling peaks of similar intensity, whatever their months of occurrence. In contrast, OFU is strengthened when wind peaks mainly occur during the July-August period. This could be due to a more intense offshore circulation (eastward jet and cyclonic gyre, which contributes more to OFU strength than for SCU) during this period, and will be examined in a future study. Second, mesoscale structures also modulate the interannual variability of wind-induced SCU and OFU. Depending on the number of AC/C dipoles along the coast and on the position of the associated eastward currents, SCU can be more or less strong. Similarly, the occurrence, intensity and position of cyclonic eddies north of the eastward jet also modulates OFU intensity.

Our simulation also confirmed that upwelling can develop along the northern part of the Vietnamese coast, as shown for the first time by Da et al. (2019) from AVHRR SST satellite data and from a 1/12° simulation for summer 1998. The high resolution of our simulation (~1 km over BoxNC) allowed to better understand which factors trigger the interannual variability of NCU. This variability is not driven by the same processes as SCU and OFU, i.e. intensity of summer wind and summer circulation, but can rather be explained by the interactions between wind and small mesoscale structures and circulation in the coastal area. In agreement with observations of Ngo and Hsin (2021), who concluded that conditions favorable to SCU and OFU were unfavorable to NCU, and vice versa, we first identified 2 situations. They correspond to cases where strong (weak) summer wind and offshore circulation favorable (unfavorable) to OFU and SCU strengthen (weaken) alongshore currents and weaken (strengthen) offshore currents along the northern part of the coast, thus offshore advection of cold water that could result from Ekman transport, resulting in weak (strong) NCU. Second, we also identified situations where wind conditions favorable to SCU and OFU are also favorable to NCU, due to the development of multiple dipoles and eastward jets ; and the opposite (unfavorable for the 3 areas), due to weak wind and to an alongshore northward current all along the coast. Similar summer wind conditions can therefore result in very contrasted NCU intensity, and conversely opposite wind conditions can result in similar NCU intensity.

Last, our study revealed that upwelling also develops offshore the Mekong delta, along the western flank of the northeastward current. As for SCU and OFU, the interannual variability of MKU intensity is mostly driven by the interannual variability of the wind-induced summer circulation in the offshore region. However, contrary to what is

https://doi.org/10.5194/os-2021-121
Preprint. Discussion started: 7 January 2022

concluded for SCU, OFU and NCU, it is hardly modulated by the influence of mesoscale dynamics of strong chaotic nature. The spatial structure of currents and upwelling over boxMK is indeed very stable, being presumably constrained by non-interannually-varying factors. Fang et al. (2012) also showed that this segment of the summer circulation is stable at the interannual scale, whereas the northern and eastern parts are much more unstable. Detailed mechanisms involved in MKU functioning and variability, in particular bathymetry but also tides, will be examined in a future study.

Da et al. (2019) revealed through their 1/12° simulation the impact of OIV on interannual variability of upwelling, using an indicator integrated over the whole SVU area. Our results highlighted the contribution of high frequency and mesoscale ocean dynamics and coastal circulation of strong chaotic nature to the interannual variability of SCU, OFU, and more particularly, NCU. Our high-resolution configuration will now be used to study the chaotic vs. forced component of ocean dynamics at different scales, and their impact on the daily and intraseasonal to interannual variability of the SVU over its different areas of development.

Last, this numerical tool can be coupled with biogeochemical models (Herrmann et al. 2014, 2017, Ulses et al. 2016) or used for applied purposes such as pollution monitoring (Estournel et al. 2012, Masumoto et al. 2012, Belharet et al. 2016). It is openly available for the scientific community willing to investigate the functioning, variability and influence of ocean dynamics in the area.

Code and data availability

The SYMPHONIE model is available on the webpage of the SIROCCO group, https://sirocco.obs-mip.fr/. Outputs of the simulation performed over the period 2009-2018 over the VNC configuration are freely available upon request to the authors.

Authors Contribution

To Duy Thai, Marine Herrmann and Claude Estournel designed the experiments and To Duy Thai carried them out, with the support of Thomas Duhaut and Patrick Marsaleix. Patrick Marsaleix, Thomas Duhaut and Claude Estournel developed the model code. To Duy Thai, Trinh Bich Ngoc and Patrick Marsaleix worked on the model optimization. Bui Hong Long organized the IO-18 survey. To Duy Thai and Marine Herrmann prepared the manuscript with contributions from all co-authors.

Competing interests

The authors declare that they have no conflict of interest.

Acknowledgements

This work is a part of LOTUS international joint laboratory (lotus.usth.edu.vn). PhD studies of To Duy Thai were funded through an IRD ARTS grant and a “Bourse d’Excellence” from the French Embassy in Vietnam. Numerical simulations were performed using CALMIP HPC facilities (project P13120) and the cluster OCCIGEN from the CINES group (project DARI A0080110098). IO-18 campaign belongs to "Study on processes of air-sea-land interactions and environmental variations of Bien Dong in the context of climate change within the framework of IOC\WESTPAC"

https://doi.org/10.5194/os-2021-121
Preprint. Discussion started: 7 January 2022

project, code: ĐTĐL.CN-28/17. Glider data were collected by the Vietnam Center for Oceanography (CFO, VASI) in the framework of the US-Vietnam collaboration project: "Gulf of Tonkin Circulation study" (NICOP N62909-15-1-2018), financed by the Office of Naval Research (ONR). This paper is a contribution to celebrate the 100 years Anniversary of the Institute of Oceanography, Vietnam Academy of Science and Technology.

References

Ablain, M., Cazenave, A., Larnicol, G., Balmaseda, M., Cipollini, P., Faugère, Y., Fernandes, M. J., Henry, O., Johannessen, J. A., Knudsen, P., Andersen, O., Legeais, J., Meyssignac, B., Picot, N., Roca, M., Rudenko, S., Scharffenberg, M. G., Stammer, D., Timms, G., and Benveniste, J. (2015). Improved sea level record over the satellite altimetry era (1993–2010) from the Climate Change Initiative project. Ocean Science, 11(1), 67–82. https://doi.org/10.5194/os-11-67-2015

Belharet, M., Estournel, C., and Charmasson, S. (2016). Ecosystem model-based approach for modeling the dynamics of 137Cs transfer to marine plankton populations: Application to the western North Pacific Ocean after the Fukushima nuclear power plant accident. Biogeosciences, 13(2), 499–516. https://doi.org/10.5194/bg-13-499-2016

Bombar, D., Dippner, J. W., Doan, H. N., Ngoc, L. N., Liskow, I., Loick-Wilde, N., and Voss, M. (2010). Sources of new nitrogen in the Vietnamese upwelling region of the South China Sea. Journal of Geophysical Research, 115(C6). https://doi.org/10.1029/2008jc005154

Boutin, J., Vergely, J. L., Marchand, S., D'Amico, F., Hasson, A., Kolodziejczyk, N., Reul, N., Reverdin, G., and Vialard, J. (2018). New SMOS Sea Surface Salinity with reduced systematic errors and improved variability. Remote Sensing of Environment, 214, 115–134. https://doi.org/10.1016/j.rse.2018.05.022

Center for International Earth Science Information Network - CIESIN - Columbia University. 2018. Gridded Population of the World, Version 4 (GPWv4): Population Density, Revision 11. Palisades, NY: NASA Socioeconomic Data and Applications Center (SEDAC). https://doi.org/10.7927/H49C6VHW.

Chao, S.-Y., Shaw, P.-T., and Wu, S. Y. (1996). El Niño modulation of the South China Sea circulation. Progress in Oceanography, 38(1), 51–93. https://doi.org/10.1016/s0079-6611(96)00010-9

Chen, C., and Wang, G. (2014). Interannual variability of the eastward current in the western South China Sea associated with the summer Asian monsoon. Journal of Geophysical Research: Oceans, 119(9), 5745–5754. https://doi.org/10.1002/2014jc010309

Chen, C., Lai, Z., Beardsley, R. C., Xu, Q., and Lin, H. (2012). Current separation and upwelling over the southeast shelf of Vietnam in the South China Sea. Journal of Geophysical Research: Oceans, 117(C03033), 1–16. https://doi.org/10.1029/2011jc007150

Costa, A., Doglioli, A. M., Marsaleix, P., and Petrenko, A. A. (2017). Comparison of in situ microstructure measurements to different turbulence closure schemes in a 3-D numerical ocean circulation model. Ocean Modelling, 120, 1–17. https://doi.org/10.1016/j.ocemod.2017.10.002

Da, N. D., Herrmann, M., Morrow, R., Niño, F., Huan, N. M., and Trinh, N. Q. (2019). Contributions of wind, ocean intrinsic variability, and ENSO to the interannual variability of the south vietnam upwelling: A modeling study. Journal of Geophysical Research: Oceans, 124(9), 6545–6574. https://doi.org/10.1029/2018jc014647

Damien, P., Bosse, A., Testor, P., Marsaleix, P., and Estournel, C. (2017). Modeling Postconvective Submesoscale Coherent Vortices in the Northwestern Mediterranean Sea. Journal of Geophysical Research: Oceans, 122(12), 9937–9961. https://doi.org/10.1002/2016jc012114

Dippner, J. W., Nguyen, K. V., Hein, H., Ohde, T., and Loick, N. (2007). Monsoon-induced upwelling off the Vietnamese

https://doi.org/10.5194/os-2021-121
Preprint. Discussion started: 7 January 2022

coast. Ocean Dynamics, 57(1), 46–62. https://doi.org/10.1007/s10236-006-0091-0

Dippner, J. W., and Loick-Wilde, N. (2011). A redefinition of water masses in the Vietnamese upwelling area. Journal of Marine Systems, 84(1–2), 42–47. https://doi.org/10.1016/j.jmarsys.2010.08.004

Estournel, C., Bosc, E., Bocquet, M., Ulses, C., Marsaleix, P., Winiarek, V., Osvath, I., Nguyen, C., Duhaut, T., Lyard, F., Michaud, H., and Auclair, F. (2012). Assessment of the amount of cesium-137 released into the Pacific Ocean after the Fukushima accident and analysis of its dispersion in Japanese coastal waters. Journal of Geophysical Research: Oceans, 117(C11), n/a-n/a. https://doi.org/10.1029/2012jc007933

Estournel, C., Marsaleix, P., and Ulses, C. (2021). A new assessment of the circulation of Atlantic and Intermediate Waters in the Eastern Mediterranean. Progress in Oceanography, 198, 102673. https://doi.org/10.1016/j.pocean.2021.102673

Fang, G., Wang, G., Fang, Y., and Fang, W. (2012). A review on the South China Sea western boundary current. Acta Oceanologica Sinica, 31(5), 1–10. https://doi.org/10.1007/s13131-012-0231-y

Fang, G., Wang, Y., Wei, Z., Fang, Y., Qiao, F., and Hu, X. (2009). Interocean circulation and heat and freshwater budgets of the South China Sea based on a numerical model. Dynamics of Atmospheres and Oceans, 47(1–3), 55–72. https://doi.org/10.1016/j.dynatmoce.2008.09.003

Fang, W., Fang, G., Shi, P., Huang, Q., and Xie, Q. (2002). Seasonal structures of upper layer circulation in the southern South China Sea from in situ observations. Journal of Geophysical Research, 107(C11). https://doi.org/10.1029/2002jc001343

Gentemann, C. L. (2004). In situ validation of Tropical Rainfall Measuring Mission microwave sea surface temperatures. Journal of Geophysical Research, 109(C4). https://doi.org/10.1029/2003jc002092

Griffies, S. M., and Hallberg, R. W. (2000). Biharmonic friction with a smagorinsky-like viscosity for use in large-scale eddy-permitting ocean models. Monthly Weather Review, 128(8), 2935–2946. https://doi.org/10.1175/1520-0493(2000)128<2935:bfwasl>2.0.co;2

Herrmann, M., Auger, P.-A., Ulses, C., and Estournel, C. (2017). Long-term monitoring of ocean deep convection using multisensors altimetry and ocean color satellite data. Journal of Geophysical Research: Oceans, 122(2), 1457–1475. https://doi.org/10.1002/2016jc011833

Herrmann, M., Duy Tung, N., Ngo-Duc, T., and Tangang, F. (2021). Climate change impact on sea surface winds in Southeast Asia. International Journal of Climatology. https://doi.org/10.1002/joc.7433

Herrmann, M., Estournel, C., Adloff, F., and Diaz, F. (2014). Impact of climate change on the northwestern Mediterranean Sea pelagic planktonic ecosystem and associated carbon cycle. Journal of Geophysical Research: Oceans, 119(9), 5815–5836. https://doi.org/10.1002/2014jc010016

Herrmann, M., Ngo-Duc, T., and Trinh-Tuan, L. (2020). Impact of climate change on sea surface wind in Southeast Asia, from climatological average to extreme events: Results from a dynamical downscaling. Climate Dynamics, 54(3–4), 2101–2134. https://doi.org/10.1007/s00382-019-05103-6

Ho, C.-R., Zheng, Q., Soong, Y. S., Kuo, N.-J., and Hu, J.-H. (2000). Seasonal variability of sea surface height in the South China Sea observed with TOPEX/Poseidon altimeter data. Journal of Geophysical Research: Oceans, 105(C6), 13981–13990. https://doi.org/10.1029/2000jc900001

Jackett, D. R., McDougall, T. J., Feistel, R., Wright, D. G., and Griffies, S. M. (2006). Algorithms for density, potential temperature, conservative temperature, and the freezing temperature of seawater. Journal of Atmospheric and Oceanic Technology, 23(12), 1709–1728. https://doi.org/10.1175/jtech1946.1

Kuo, N.-J., Zheng, Q., and Ho, C.-R. (2004). Response of Vietnam coastal upwelling to the 1997–1998 ENSO event observed by multisensor data. Remote Sensing of Environment, 89(1), 106–115.

https://doi.org/10.5194/os-2021-121
Preprint. Discussion started: 7 January 2022

https://doi.org/10.1016/j.rse.2003.10.009

Large, W. G., and Yeager, S. (2004). Diurnal to decadal global forcing for ocean and sea-ice models: The data sets and flux climatologies (No. NCAR/TN-460+STR). University Corporation for Atmospheric Research. doi:10.5065/D6KK98Q6

Leonard, B. P. (1979). A stable and accurate convective modelling procedure based on quadratic upstream interpolation. Computer Methods in Applied Mechanics and Engineering, 19(1), 59–98. https://doi.org/10.1016/0045-7825(79)90034-3

Li, Y., Han, W., and Zhang, L. (2017). Enhanced decadal warming of the Southeast Indian Ocean during the recent global surface warming slowdown. Geophysical Research Letters, 44(19), 9876–9884. https://doi.org/10.1002/2017gl075050

Li, Y., Han, W., Wilkin, J. L., Zhang, W. G., Arango, H., Zavala-Garay, J., Levin, J., and Castruccio, F. S. (2014). Interannual variability of the surface summertime eastward jet in the South China Sea. Journal of Geophysical Research: Oceans, 119(10), 7205–7228. https://doi.org/10.1002/2014jc010206

Loick, N., Dippner, J., Doan, H. N., Liskow, I., and Voss, M. (2007). Pelagic nitrogen dynamics in the Vietnamese upwelling area according to stable nitrogen and carbon isotope data. Deep Sea Research Part I: Oceanographic Research Papers, 54(4), 596–607. https://doi.org/10.1016/j.dsr.2006.12.009

Loick-Wilde, N., Bombar, D., Doan, H. N., Nguyen, L. N., Nguyen-Thi, A. M., Voss, M., and Dippner, J. W. (2017). Microplankton biomass and diversity in the Vietnamese upwelling area during SW monsoon under normal conditions and after an ENSO event. Progress in Oceanography, 153, 1–15. https://doi.org/10.1016/j.pocean.2017.04.007

Loisel, H., Vantrepotte, V., Ouillon, S., Ngoc, D. D., Herrmann, M., Tran, V., Mériaux, X., Dessailly, D., Jamet, C., Duhaut, T., Nguyen, H. H., and Van Nguyen, T. (2017). Assessment and analysis of the chlorophyll-a concentration variability over the Vietnamese coastal waters from the MERIS ocean color sensor (2002–2012). Remote Sensing of Environment, 190, 217–232. https://doi.org/10.1016/j.rse.2016.12.016

Lu, W., Oey, L.-Y., Liao, E., Zhuang, W., Yan, X.-H., and Jiang, Y. (2018). Physical modulation to the biological productivity in the summer Vietnam upwelling system. Ocean Science, 14(5), 1303–1320. https://doi.org/10.5194/os-14-1303-2018

Lyard, F., Lefevre, F., Letellier, T., and Francis, O. (2006). Modelling the global ocean tides: Modern insights from FES2004. Ocean Dynamics, 56(5–6), 394–415. https://doi.org/10.1007/s10236-006-0086-x

Marsaleix, P., Auclair, F., and Estournel, C. (2006). Considerations on open boundary conditions for regional and Coastal Ocean models. Journal of Atmospheric and Oceanic Technology, 23(11), 1604–1613. https://doi.org/10.1175/jtech1930.1

Marsaleix, P., Auclair, F., and Estournel, C. (2009). Low-order pressure gradient schemes in sigma coordinate models: The seamount test revisited. Ocean Modelling, 30(2–3), 169–177. https://doi.org/10.1016/j.ocemod.2009.06.011

Marsaleix, P., Auclair, F., Floor, J. W., Herrmann, M. J., Estournel, C., Pairaud, I., and Ulses, C. (2008). Energy conservation issues in sigma-coordinate free-surface ocean models. Ocean Modelling, 20(1), 61–89. https://doi.org/10.1016/j.ocemod.2007.07.005

Marsaleix, P., Michaud, H., and Estournel, C. (2019). 3D phase-resolved wave modelling with a non-hydrostatic ocean circulation model. Ocean Modelling, 136, 28–50. https://doi.org/10.1016/j.ocemod.2019.02.002

Masumoto, Y., Miyazawa, Y., Tsumune, D., Tsubono, T., Kobayashi, T., Kawamura, H., Estournel, C., Marsaleix, P., Lanerolle, L., Mehra, A., and Garraffo, Z. D. (2012). Oceanic dispersion simulations of 137cs released from the Fukushima Daiichi Nuclear Power Plant. Elements, 8(3), 207–212. https://doi.org/10.2113/gselements.8.3.207

Michaud, H., Marsaleix, P., Leredde, Y., Estournel, C., Bourrin, F., Lyard, F., Mayet, C., and Ardhuin, F. (2012). Three-dimensional modelling of wave-induced current from the surf zone to the inner shelf. Ocean Science, 8(4), 657–681. https://doi.org/10.5194/os-8-657-2012

https://doi.org/10.5194/os-2021-121
Preprint. Discussion started: 7 January 2022

Ngo, M., and Hsin, Y. (2021). Impacts of wind and current on the interannual variation of the summertime upwelling off southern Vietnam in the South China Sea. Journal of Geophysical Research: Oceans, 126(6). https://doi.org/10.1029/2020jc016892

Nguyen-Duy, T., Ayoub, N. K., Marsaleix, P., Toublanc, F., De Mey-Frémaux, P., Piton, V., Herrmann, M., Duhaut, T., Tran, M. C., and Ngo-Duc, T. (2021). Variability of the Red River plume in the Gulf of Tonkin as revealed by numerical modeling and clustering analysis. Frontiers in Marine Science, 8. https://doi.org/10.3389/fmars.2021.772139

Pairaud, I., Staquet, C., Sommeria, J., and Mahdizadeh, M. M. (2010). Generation of harmonics and sub-harmonics from an internal tide in a uniformly stratified fluid: Numerical and laboratory experiments. In IUTAM Symposium on Turbulence in the Atmosphere and Oceans (pp. 51–62). Springer Netherlands. http://dx.doi.org/10.1007/978-94-007-0360-5_5

Pairaud, I. L., Lyard, F., Auclair, F., Letellier, T., and Marsaleix, P. (2008). Dynamics of the semi-diurnal and quarter-diurnal internal tides in the Bay of Biscay. Part 1: Barotropic tides. Continental Shelf Research, 28(10–11), 1294–1315. https://doi.org/10.1016/j.csr.2008.03.004

Piton, V., Herrmann, M., Marsaleix, P., Duhaut, T., Ngoc, T. B., Tran, M. C., Shearman, K., and Ouillon, S. (2021). Influence of winds, geostrophy and typhoons on the seasonal variability of the circulation in the Gulf of Tonkin: A high-resolution 3D regional modeling study. Regional Studies in Marine Science, 45, 101849. https://doi.org/10.1016/j.rsma.2021.101849

Qu, T., and Song, Y. T. (2009). Mindoro Strait and Sibutu Passage transports estimated from satellite data. Geophysical Research Letters, 36(9). https://doi.org/10.1029/2009gl037314

Qu, T. (2000). Upper-Layer circulation in the South China Sea. Journal of Physical Oceanography, 30(6), 1450–1460. https://doi.org/10.1175/1520-0485(2000)030<1450:ULCITS>2.0.CO;2

Ray, R. D., and Zaron, E. D. (2015). M2 internal tides and their observed wavenumber spectra from satellite altimetry. Journal of Physical Oceanography, 46(1), 3–22. https://doi.org/10.1175/jpo-d-15-0065.1

Reffray, G., Fraunié, P., and Marsaleix, P. (2004). Secondary flows induced by wind forcing in the Rhône region of freshwater influence. Ocean Dynamics, 54(2), 179–196. https://doi.org/10.1007/s10236-003-0079-y

Rogowski, P., Zavala-Garay, J., Shearman, K., Terrill, E., Wilkin, J., and Lam, T. H. (2019). Air-Sea-Land forcing in the Gulf of Tonkin: Assessing seasonal variability using modern tools. Oceanography, 32(2), 150–161. https://doi.org/10.5670/oceanog.2019.223

Shaw, P.-T., Chao, S.-Y., and Fu, L.-L. (1999). Sea surface height variations in the South China Sea from satellite altimetry. Oceanologica Acta, 22(1), 1–17. https://doi.org/10.1016/s0399-1784(99)80028-0

Siddorn, J. R., and Furner, R. (2013). An analytical stretching function that combines the best attributes of geopotential and terrain-following vertical coordinates. Ocean Modelling, 66, 1–13. https://doi.org/10.1016/j.ocemod.2013.02.001

Siew, J. H., Tangang, F. T., and Juneng, L. (2013). Evaluation of CMIP5 coupled atmosphere-ocean general circulation models and projection of the Southeast Asian winter monsoon in the 21st century. International Journal of Climatology, 34(9), 2872–2884. https://doi.org/10.1002/joc.3880

Toublanc, F., Ayoub, N. K., Lyard, F., Marsaleix, P., and Allain, D. J. (2018). Tidal downscaling from the open ocean to the coast: A new approach applied to the Bay of Biscay. Ocean Modelling, 124, 16–32. https://doi.org/10.1016/j.ocemod.2018.02.001

Trinh, B. N. (2020). Cycles de l'eau, de la chaleur et du sel en Mer de Chine Méridionale, de la variation saisonnière à la variabilité interannuelle : modélisation océanique à haute résolution et à bilan fermé [Doctoral dissertation]. Université de Toulouse, Toulouse, France.

Ulses, C., Auger, P.-A., Soetaert, K., Marsaleix, P., Diaz, F., Coppola, L., Herrmann, M. J., Kessouri, F., and Estournel,

https://doi.org/10.5194/os-2021-121
Preprint. Discussion started: 7 January 2022

C. (2016). Budget of organic carbon in the North-Western Mediterranean open sea over the period 2004-2008 using 3-D coupled physical-biogeochemical modeling. Journal of Geophysical Research: Oceans, 121(9), 7026–7055. https://doi.org/10.1002/2016jc011818

UK Met Office. 2005. OSTIA L4 SST Analysis. Ver. 1.0. PO.DAAC, CA, USA. Dataset accessed [YYYY-MM-DD] at https://doi.org/10.5067/GHOST-4FK01

Uu, D. V., and Brankart, J.-M. (1997). Seasonal variation of temperature and salinity fields and water masses in the Bien Dong (South China) sea. Mathematical and Computer Modelling, 26(12), 97–113. https://doi.org/10.1016/s0895-7177(97)00243-4

Wang, B., LinHo, Zhang, Y., and Lu, M.-M. (2004). Definition of South China Sea monsoon onset and commencement of the East Asia summer monsoon*. Journal of Climate, 17(4), 699–710. https://doi.org/10.1175/2932.1

Wang, Y.-L., and Wu, C.-R. (2020). Nonstationary El Niño teleconnection on the post-summer upwelling off Vietnam. Scientific Reports, 10(1). https://doi.org/10.1038/s41598-020-70147-2

Woo, H.-J., and Park, K.-A. (2020). Inter-Comparisons of daily sea surface temperatures and in-situ temperatures in the coastal regions. Remote Sensing, 12(10), 1592. https://doi.org/10.3390/rs12101592

Wu, X., Okumura, Y. M., and DiNezio, P. N. (2019). What controls the duration of El Niño and La Niña events? Journal of Climate, 32(18), 5941–5965. https://doi.org/10.1175/jcli-d-18-0681.1

Wyrtki, K. (1961). Scientific Results of Marine Investigations of the South China Sea and the Gulf of Thailand 1959–1961 Physical Oceanography of the Southeast Asian Waters. NAGA report 2, 195

Xie, S.-P., Chang, C.-H., Xie, Q., and Wang, D. (2007). Intraseasonal variability in the summer South China Sea: Wind jet, cold filament, and recirculations. Journal of Geophysical Research, 112(C10). https://doi.org/10.1029/2007jc004238

Xie, S.-P., Xie, Q., Wang, D., and Liu, W. T. (2003). Summer upwelling in the South China Sea and its role in regional climate variations. Journal of Geophysical Research, 108(C8). https://doi.org/10.1029/2003jc001867

Xu, X., (1982). The general descriptions of the horizontal circulation in the South China Sea. In: In Proceedings of the 1980 Symposium on Hydrometeorology, Chinese Society of Oceanology and Limnology. Science Press, pp. 137–145.

Yu, Y., Zhang, H.-R., Jin, J., and Wang, Y. (2019). Trends of sea surface temperature and sea surface temperature fronts in the South China Sea during 2003–2017. Acta Oceanologica Sinica, 38(4), 106–115. https://doi.org/10.1007/s13131-019-1416-4

Zeng, L., Chassignet, E. P., Schmitt, R. W., Xu, X., and Wang, D. (2018). Salinification in the South China Sea since late 2012: A reversal of the freshening since the 1990s. Geophysical Research Letters, 45(6), 2744–2751. https://doi.org/10.1002/2017gl076574

Zeng, L., Timothy Liu, W., Xue, H., Xiu, P., and Wang, D. (2014). Freshening in the South China Sea during 2012 revealed by Aquarius and in situ data. Journal of Geophysical Research: Oceans, 119(12), 8296–8314. https://doi.org/10.1002/2014jc010108

Zeng, L., Wang, D., Xiu, P., Shu, Y., Wang, Q., and Chen, J. (2016). Decadal variation and trends in subsurface salinity from 1960 to 2012 in the northern South China Sea. Geophysical Research Letters, 43(23), 12,181-12,189. https://doi.org/10.1002/2016gl071439

Zheng, Z.-W., Zheng, Q., Kuo, Y.-C., Gopalakrishnan, G., Lee, C.-Y., Ho, C.-R., Kuo, N.-J., and Huang, S.-J. (2016). Impacts of coastal upwelling off east Vietnam on the regional winds system: An air-sea-land interaction. Dynamics of Atmospheres and Oceans, 76, 105–115. https://doi.org/10.1016/j.dynatmoce.2016.10.002

https://doi.org/10.5194/os-2021-121
Preprint. Discussion started: 7 January 2022

Tables

Table 1. Information about in-situ measurements used in this study

Name of dataset	Period	Number of stations/points	Type of sensor
ARGO	01.01.2009-31.12.2018	3675	CTD, (T,S profiles)
ALIS -TSG	22.05-21.07.2014	573,803 (1 point every ~40s)	TSG (SSS, SST)
Glider	22.01-16.05.2017	552	CTD (T,S profiles)
IO-18	12.09-25.09.2018	43	CTD (T,S profiles)

835

https://doi.org/10.5194/os-2021-121
Preprint. Discussion started: 7 January 2022

Table 2 : From 1st to last line : temporal mean and standard deviation of UIy,boxN over 2009-2018 for each box and coefficient of variation CV, mean of average wind stress averaged over June-September over each box, mean of integrated positive vorticity over BoxOF, correlations (correlation coefficient and associate p-values) between time series of significant factors : yearly upwelling index over each box vs. yearly upwelling index over other boxes, vs. average wind stress averaged over June-September (JJAS) and July-August (JA) over each box, vs. integrated positive vorticity over BoxOF ; average JJAS wind stress over each box vs. average JJAS wind stress over other boxes and vs. integrated positive vorticity over BoxOF. Correlations significant at more than 99% (p<0.01) are highlighted in bold.

	BoxNC	BoxSC	BoxOF	BoxMK
$UI_{y,boxN}$ mean (°C)	0.14	0.42	0.09	0.07
$UI_{y,boxN}$ STD (°C)	0.14	0.42	0.09	0.06
CV (%)	71	53	126	85
Mean of $WS_{JJAS,boxN}$ ($N.m^{-3}$)	0.03	0.09	0.08	0.07
Mean of $\zeta_{+,OF}$ (s^{-1})	$1.95x10^{-6}$			
Correlation between :	$UI_{y,NC}$	$UI_{y,SC}$	$UI_{y,OF}$	$UI_{y,MK}$
$UI_{y,SC}$ (°C)	+0.01(0.98)	**1**	**+0.73(0.02)**	**+0.83(0.00)**
$UI_{y,OF}$ (°C)	-0.26(0.47)	**+0.73(0.02)**	**1**	**+0.92(0.00)**
$UI_{y,MK}$ (°C)	-0.19(0.59)	**+0.83(0.00)**	**+0.92(0.00)**	**1**
$WS_{JJAS,NC}$ ($N.m^{-3}$)	-0.10(0.77)	-0.41(0.24)	+0.23(0.53)	+0.07(0.85)
$WS_{JJAS,SC}$ ($N.m^{-3}$)	-0.13(0.73)	**+0.85(0.00)**	**+0.76(0.01)**	**+0.84(0.00)**
$WS_{JJAS,OF}$ ($N.m^{-3}$)	-0.19(0.61)	**+0.81(0.00)**	**+0.77(0.01)**	**+0.80(0.01)**
$WS_{JJAS,MK}$ ($N.m^{-3}$)	-0.08(0.82)	**+0.78(0.01)**	**+0.63(0.05)**	**+0.72(0.02)**
$WS_{JA,NC}$ ($N.m^{-3}$)	+0.07(0.92)	+0.12(0.62)	+0.54(0.11)	+0.38(0.28)
$WS_{JA,SC}$ ($N.m^{-3}$)	-0.15(0.69)	**+0.70(0.03)**	**+0.84(0.00)**	**+0.84(0.00)**
$W_{JA,OF}$ ($N.m^{-3}$)	-0.15(0.67)	**+0.69(0.03)**	**+0.84(0.00)**	**+0.82(0.00)**
$W_{JA,MK}$ ($N.m^{-3}$)	-0.11(0.77)	**+0.72(0.02)**	**+0.78(0.01)**	**+0.82(0.00)**
Integrated Positive vorticity OF $\zeta_{+,OF}$ (s^{-1})	-0.28(0.43)	**+0.60(0.07)**	**+0.69(0.03)**	**+0.74(0.01)**
Correlation between :	$WS_{JJAS,NC}$	$WS_{JJAS,SC}$	$WS_{JJAS,OF}$	$WS_{JJAS,MK}$
$WS_{JJAS,SC}$ ($N.m^{-3}$)	-0.20(0.58)	**1**	**0.99(0.00)**	**+0.97(0.00)**
$WS_{JJAS,OF}$ ($N.m^{-3}$)	-0.19(0.60)	**0.99(0.00)**	**1**	**+0.96(0.00)**
$WS_{JJAS,MK}$ ($N.m^{-3}$)	-0.31(0.39)	**0.97(0.00)**	**+0.96(0.00)**	**1**
$\zeta_{+,OF}$ (s^{-1})	+0.02(0.95)	**+0.89(0.00)**	**+0.89(0.00)**	**+0.81(0.01)**

https://doi.org/10.5194/os-2021-121
Preprint. Discussion started: 7 January 2022

845 **Figures**

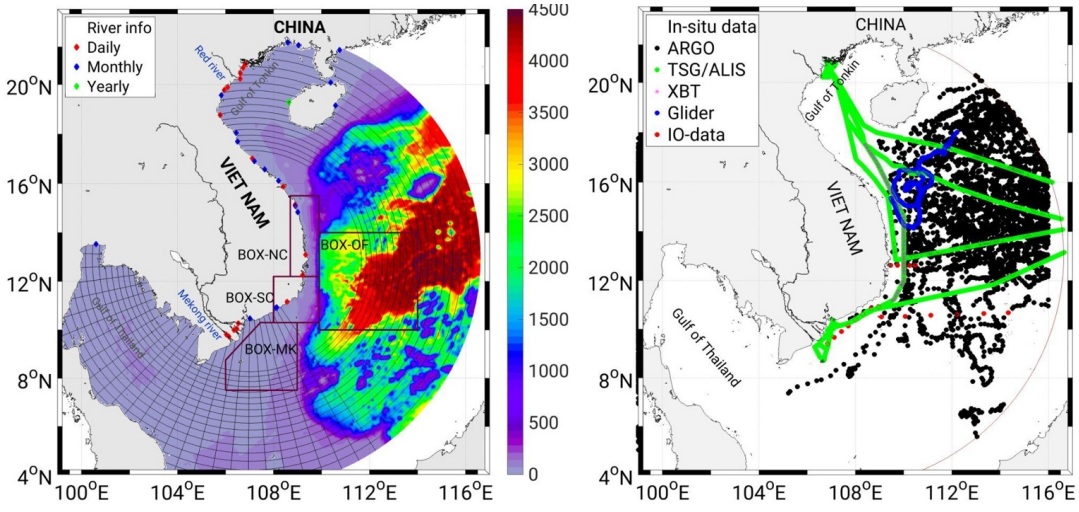

Figure 1. (Left) Characteristics of the orthogonal curvilinear computational grid (black lines, not all points are shown for visibility purposes) and bathymetry (colors, m, *GEBCO_2014*) used over the VNC configuration of the
850 **SYMPHONIE model. Dots show the location of rivers for which we used daily (red), monthly (blue) and yearly climatology (green) discharge values. Black boxes show the location of the 4 boxes used for the study of VNU. (Right) Location of *in-situ* data available over the VNC domain: ARGO buoys (black), ALIS R/V campaign (TSG: green), IO-18 data (red), and glider data (blue).**

https://doi.org/10.5194/os-2021-121
Preprint. Discussion started: 7 January 2022

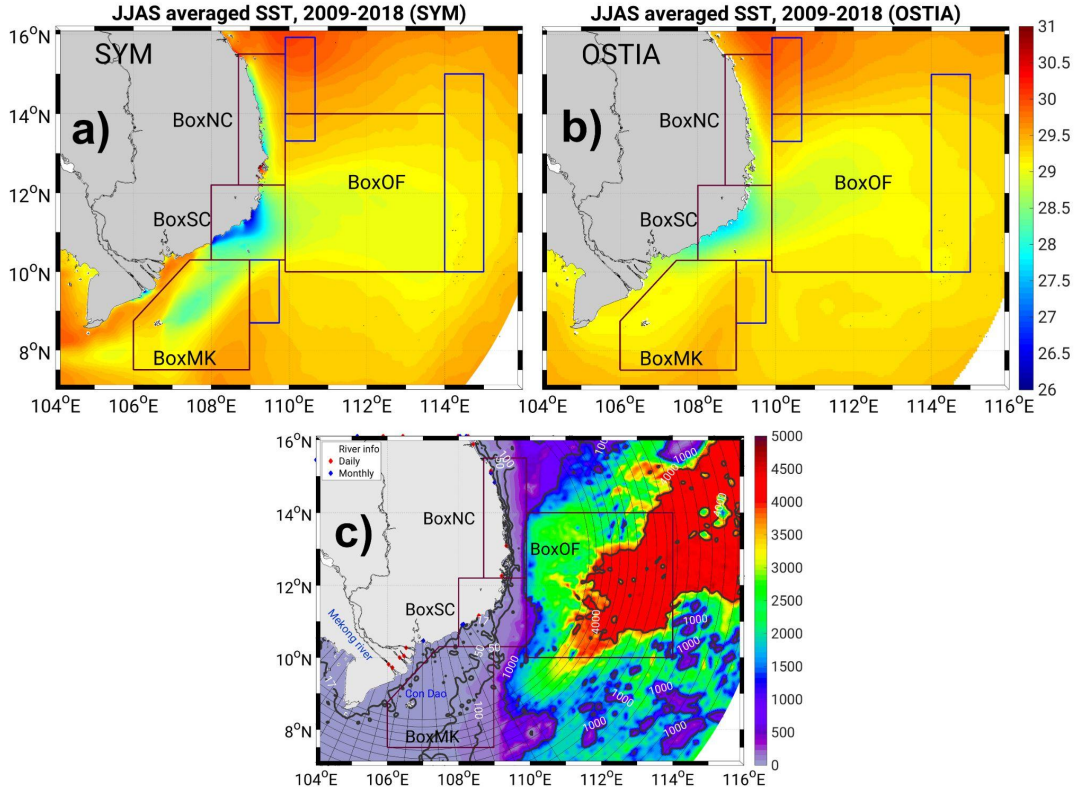

Figure 2 : JJAS average over 2009-2018 of simulated (a) and observed (b) SST (°C) over the SVU region, and (c) bathymetry of the SVU region. Black boxes show the 4 upwelling areas, and blue rectangles in a,b show the corresponding reference boxes. Coordinates of the boxes : BoxNC (12.2-15.5°N; 108.7-109.9°E), BoxSC (10.3-12.2°N; 108-109.9°E), BoxOF (10-14°N; 109.9-114°E), BoxMK (at depth > 17m, 7.5-10.3°N; 106-109°E). Ref_{NC} (13.3-15.9°N; 109.9-110.7°E), $Ref_{SC\&MK}$ (8.7-10.3°N; 109-109.7°E), Ref_{OF} (10-15°N; 114-115°E)

https://doi.org/10.5194/os-2021-121
Preprint. Discussion started: 7 January 2022

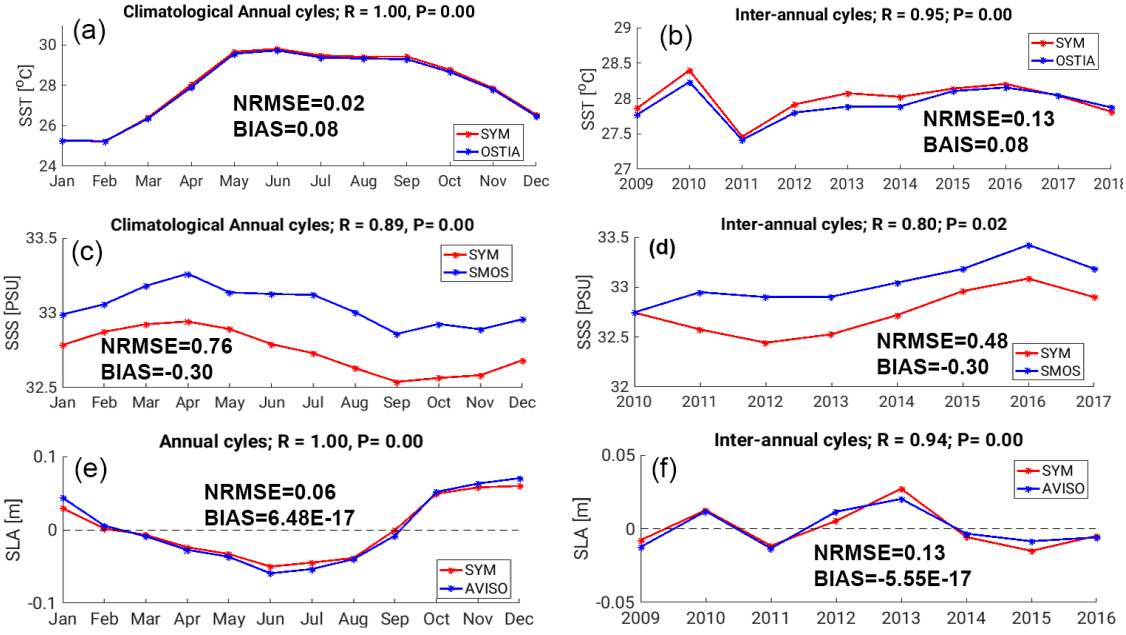

865 **Figure 3. Climatological monthly time series (left) and interannual yearly time series (right) of simulated (red) and observed (blue) SST (a,b, °C), SSS (c,d) and SLA (e,f, m) averaged over the VNC domain. Correlation (correlation coefficient R and p-value P), NRMSE and bias of simulated vs. observed values are indicated.**

https://doi.org/10.5194/os-2021-121
Preprint. Discussion started: 7 January 2022

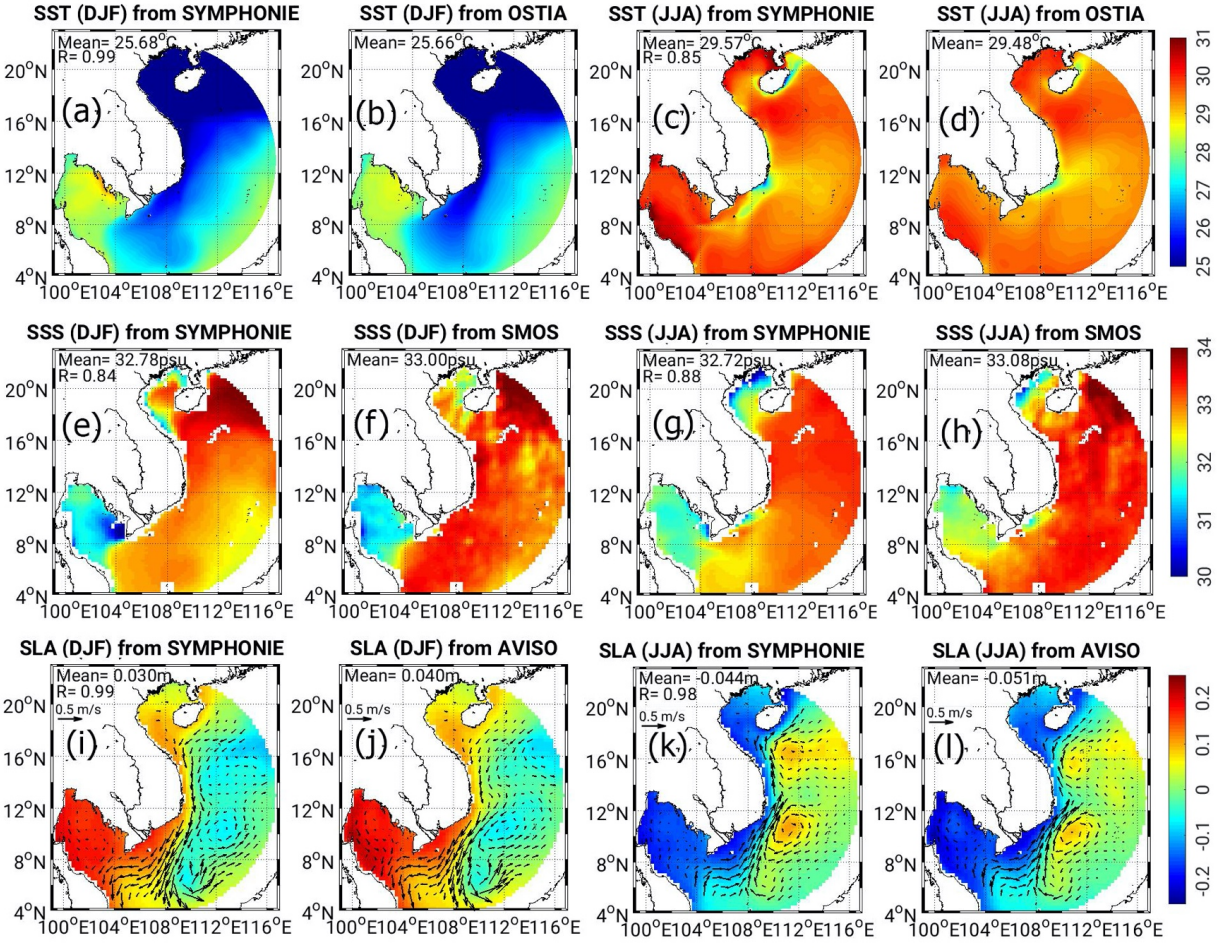

870 **Figure 4 : Spatial distribution of simulated and observed winter (DJF) and summer (JJA) climatological averages of SST (a,b,c,d, °C), SSS (e, f, g, h), SLA (i,j,k,l, m) and total surface geostrophic current (m.s^{-1}), and spatial correlation coefficient R (here the p-value is always smaller than 0.01)**

https://doi.org/10.5194/os-2021-121
Preprint. Discussion started: 7 January 2022

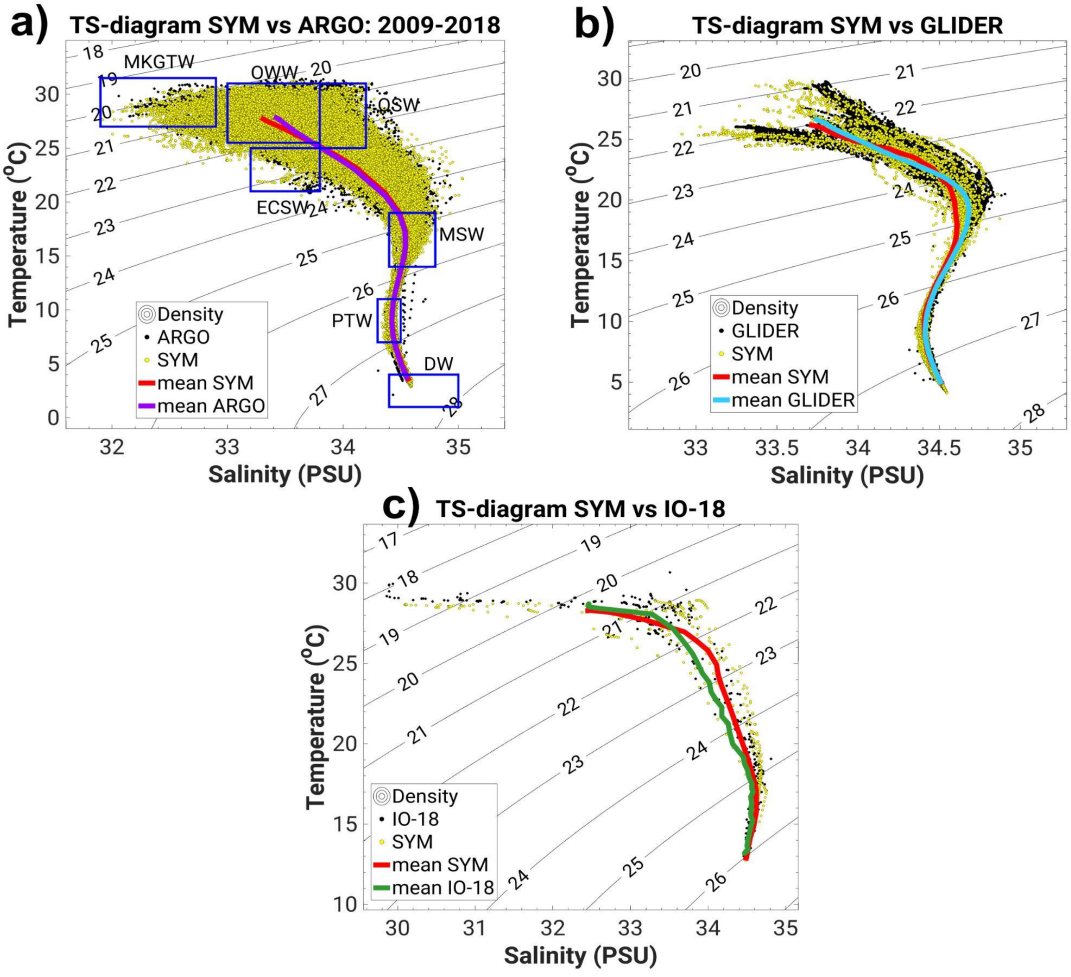

875

Figure 5 : TS-diagram built from ARGO (a, black dots and purple for mean), GLIDER (b, black dots and cyan for mean), IO-18 (c, black dots and green for mean) observations and from SYMPHONIE (yellow dots and red for mean) colocalized outputs. Blue rectangles represent water masses in the SCS (Uu and Brankard 1997,
880 **Dippner et al. 2011) : MKGTW (Mekong & Gulf of Thailand Water), OWW (Offshore Warm Water), OSW (Offshore Salty Water), ECSW (East China Sea Water), MSW (Maximum Salinity Water), PTW (Permanent Thermocline Water), DW (Deep Water).**

https://doi.org/10.5194/os-2021-121
Preprint. Discussion started: 7 January 2022

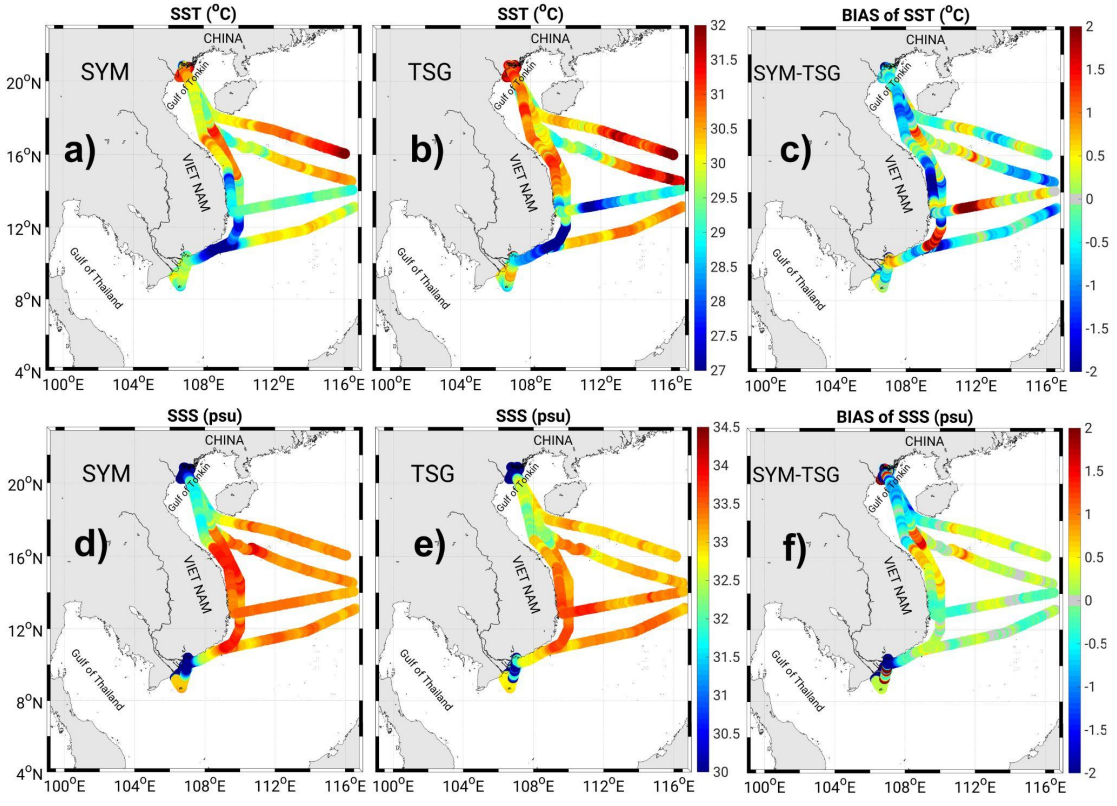

885

Figure 6 : Values of SST (top) and SSS (bottom) from (a,d) ALIS-TSG trajectory during summer 2014 and from (b,e) SYMPHONIE colocalized outputs, and (c,f) bias between SYMPHONIE and ALIS-TSG.

https://doi.org/10.5194/os-2021-121
Preprint. Discussion started: 7 January 2022

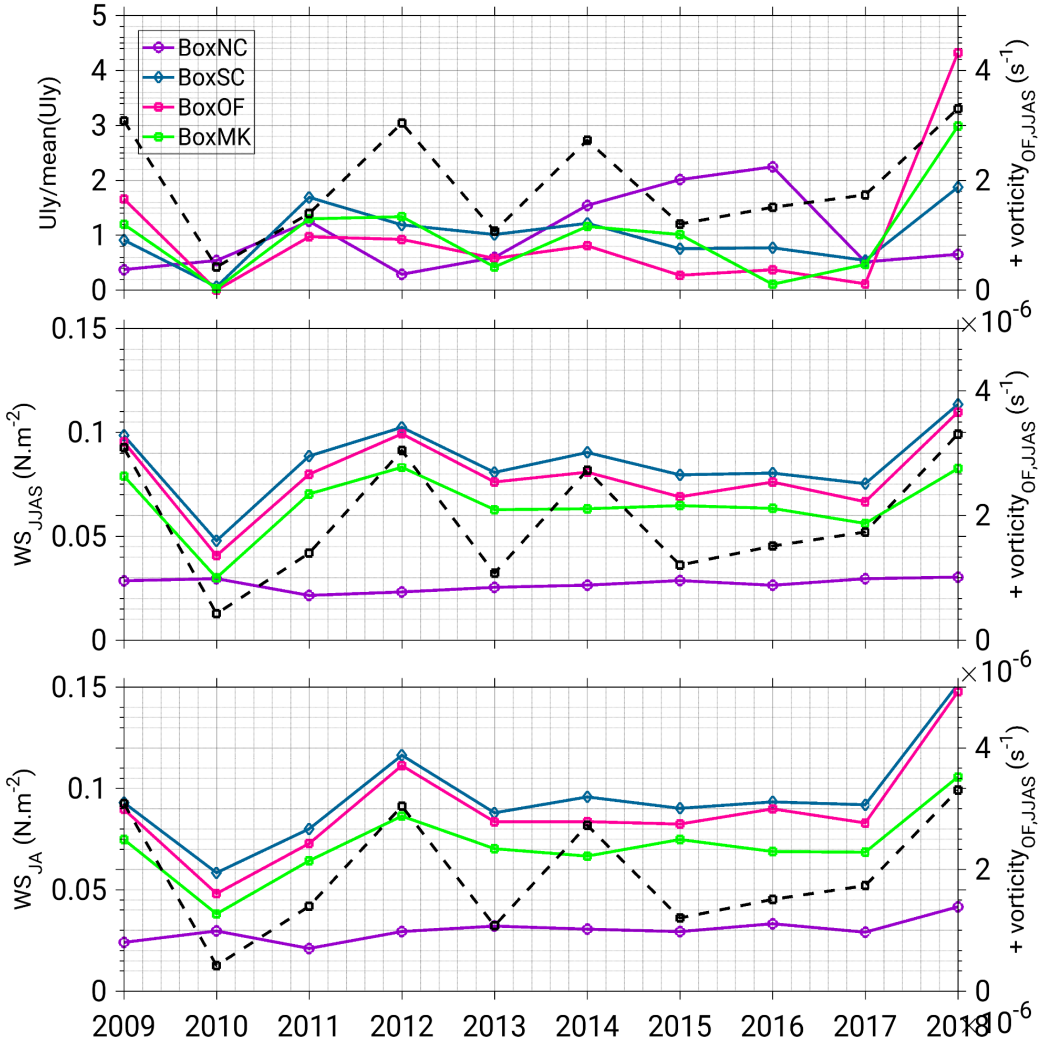

Figure 7 : Interannual time series of normalized yearly upwelling index (top), average JJAS (middle) and JA (bottom) wind stress ($N.m^{-2}$) over each upwelling box (BoxNC: purple ; BoxSC: blue; BoxOF: pink; BoxMK: green). The black dashed curve shows the integrated positive summer surface current vorticity over BoxOF (s^{-1}).

https://doi.org/10.5194/os-2021-121
Preprint. Discussion started: 7 January 2022

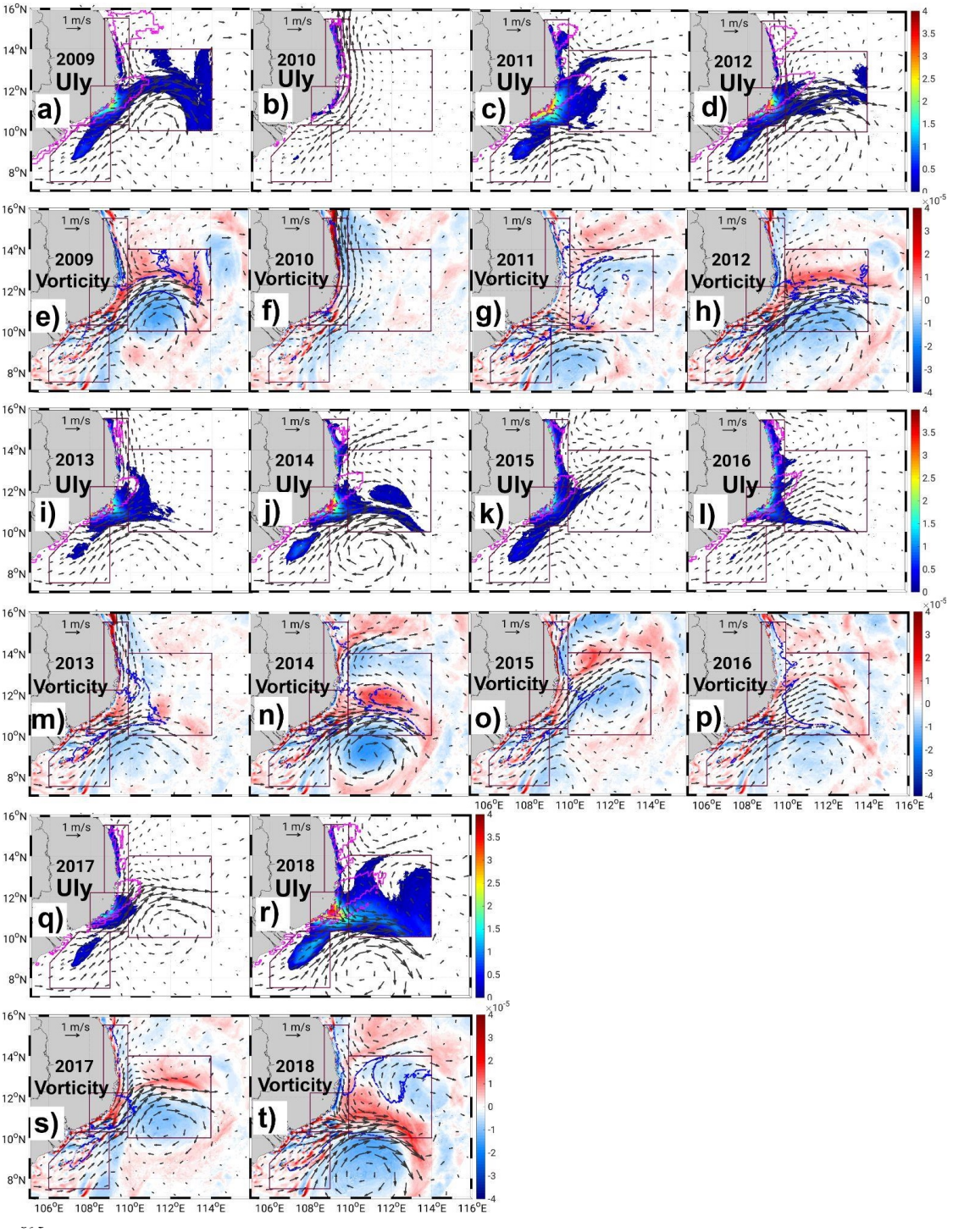

Figure 8 : Maps of spatial yearly upwelling index (°C, a,b,c,d,i,j,k,l,q,r) and of speed and direction (arrows, m.s^{-1}) and vorticity (colors, s^{-1}) of JJAS averaged surface current (e,f,g,h,m,n,o,p,s,t) for each year of the simulation.

https://doi.org/10.5194/os-2021-121
Preprint. Discussion started: 7 January 2022

Ocean Science
Discussions
Open Access
EGU

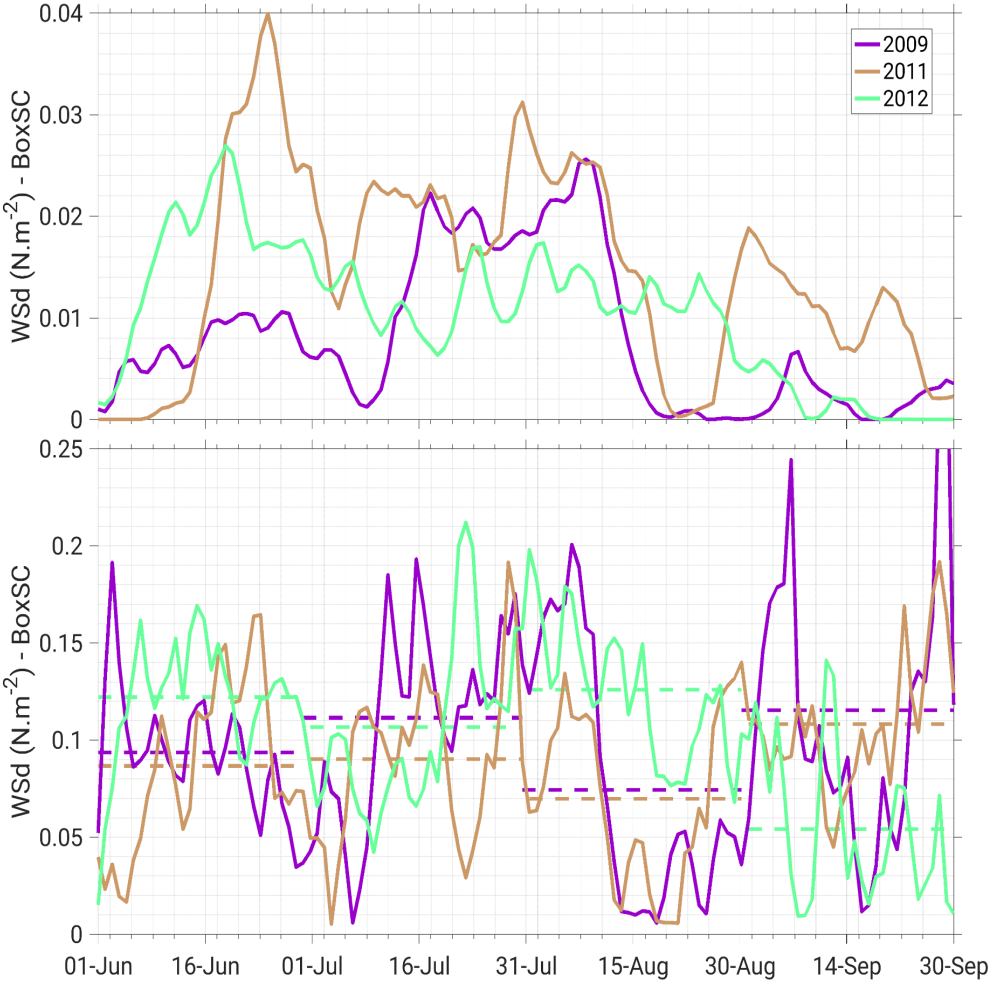

900

Figure 9 : Time series of daily upwelling index (top) and average daily (plain line) and monthly (dashed line) wind stress (bottom) over BoxSC between June and September for years 2009 (purple), 2011 (orange) and 2012 (green).

https://doi.org/10.5194/os-2021-121
Preprint. Discussion started: 7 January 2022

Ocean Science
Discussions
Open Access
EGU

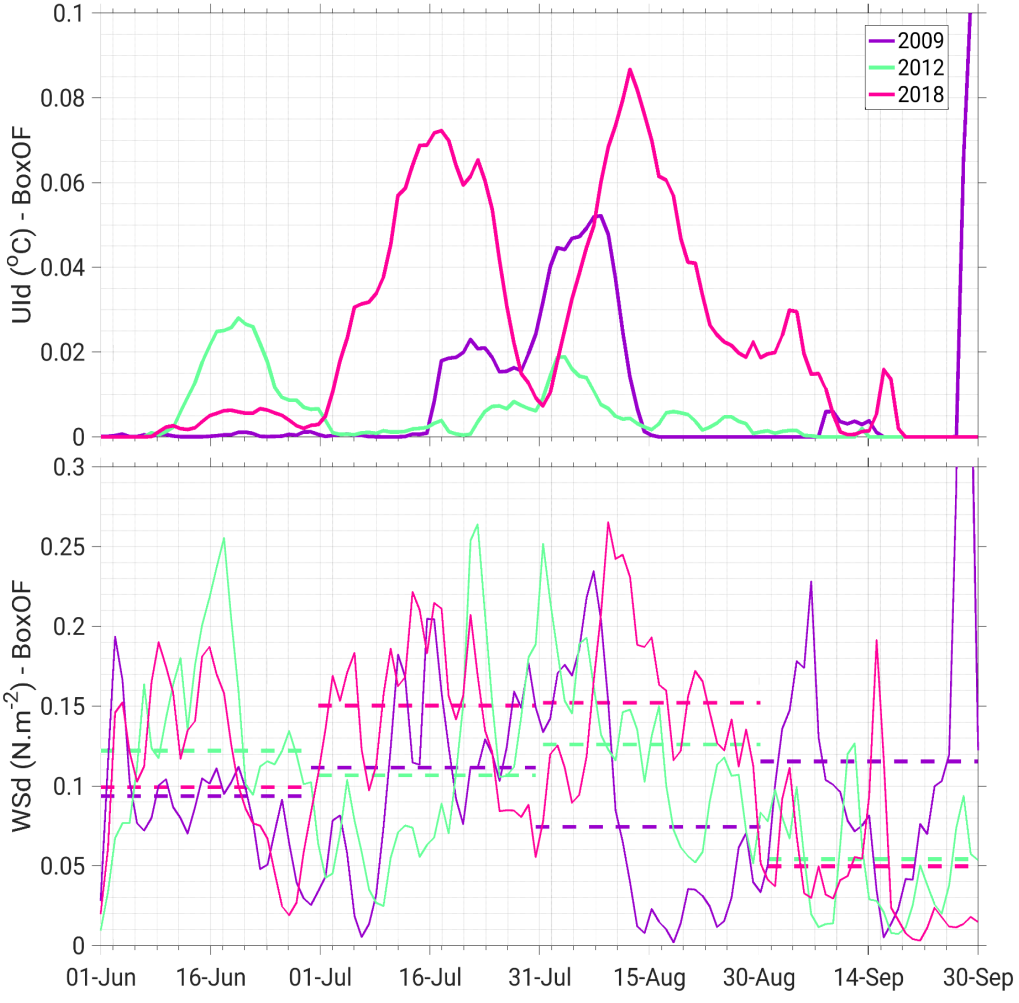

905 **Figure 10 : Same as Figure 9 for BoxOF and years 2009 (purple), 2012 (green) and 2018 (magenta).**